Thin–Walled Structures 200 (2024) 111908

Contents lists available at ScienceDirect

Thin-Walled Structures

journal homepage: www.elsevier.com/locate/tws

Full length article

A new model for calculating the ultimate shear resistance of steel I-section girders

Luke Lapira *, Leroy Gardner, M. Ahmer Wadee

Department of Civil and Environmental Engineering, Imperial College London, London, UK

ARTICLE INFO

Keywords:
Thin webs
Shear
Girders
Eurocode
Finite element analysis
I-section

ABSTRACT

The design resistance in shear of thin-walled I-sections has elicited numerous theories over the past decades. While there is a consensus on the post-buckling tension-field action that increases the ultimate resistance of thin webs in shear, the mechanism governing this tension-field action still remains debated. Presently, four constituent components for the shear resistance of I-sections are identified: (1) the resistance of the isolated web subject to a pure shear stress; (2) an increase in the web buckling stress due to flexural restraints provided by the flanges; (3) an increased web post-buckling resistance due to membrane restraint provided by the flanges; and (4) a direct contribution from the flanges to the shear resistance of the I-section. Each of these components is examined through parametric studies using finite element (FE) models analysed within Abaqus that are validated against published experimental results. A new design methodology for the resistance of I-sections in shear is presented, with closed-form expressions developed for each of the four component contributions. When compared with the current approach within EN 1993-1-5, the proposed formulae predict the shear resistance of the cross-section with greater accuracy and consistency.

1. Introduction

Built-up I-sections, also referred to as plate girders, are commonplace in practical engineering designs owing to their structural efficiency and ease of fabrication. The efficiency stems from the ability to feature thin, deep webs to separate the flanges and hence maximise the bending resistance and flexural stiffness of the section while minimising the self-weight. The design of such slender webs is governed by local and shear buckling, but their behaviour is characterised by strong post-buckling stability, often referred to as 'tension-field action' [1], and the beneficial influence of the stiffeners.

To elaborate on this matter, consider an I-section subjected to a pure shear stress, as depicted in Fig. 1(a). During the initial stages of loading, the web of the I-section is in a state of pure shear with the principal stresses σ_1 and σ_2 being aligned at an angle $\theta_0 = 45°$ to the x-axis. Before the critical buckling stress is reached, σ_1 and σ_2 are purely tensile and compressive stresses, respectively, of equal magnitude yet acting in the directions indicated in Fig. 1(a). The presence of compressive stresses within thin-walled elements inevitably leads to buckling instability [2–6]. However, the tensile stresses in the web increase further after buckling, forming the prominent tension band across the diagonal, which of course has been observed in many experimental studies [1,2,7,8].

This post-buckling tension field action is widely accepted in the design of aerospace and civil engineering structures [9]; however, differences emerge between design methods in the degree to which this tensile stress can develop, in the anchoring mechanism for the additional tensile stress and in the flange contribution to the shear resistance. Hingnekar and Vyavahare [9] have already presented a thorough literature review of the prominent shear design models developed over the past decades; thus, only a short summary of the three most prominent design models is presented currently. Wagner's model, depicted in Fig. 1(b), considered the web to act purely in tension with all the additional stresses resisted by rigid stiffeners at the supports [2]. This is widely accepted as an 'upper bound' solution that is not practically achievable [10]. For civil engineering structures, Basler [3] developed a partial tension field theory by considering the additional anchorage provided by the transverse stiffeners, since the flanges were not considered to be sufficiently stiff to anchor the additional tensile stresses in the web, as depicted in Fig. 1(c). Conversely, the 'Cardiff' model of Porter et al. [4] and Höglund's rotated stress-field model [5] asserted that the flanges do contribute to the load-carrying mechanism, as shown in Fig. 1(d), and thus proposed appropriate formulae to calculate this contribution.

Höglund's model [11], and its adaptation in EN 1993-1-5 [12], considers the contributions of the web through the rotated stress field

* Correspondence to: Department of Civil, Environmental and Geomatic Engineering, University College London, London, UK.
E-mail addresses: l.lapira@ucl.ac.uk (L. Lapira), leroy.gardner@imperial.ac.uk (L. Gardner), a.wadee@imperial.ac.uk (M.A. Wadee).

https://doi.org/10.1016/j.tws.2024.111908
Received 7 September 2023; Received in revised form 25 March 2024; Accepted 11 April 2024
Available online 16 April 2024
0263-8231/© 2024 The Author(s). Published by Elsevier Ltd. This is an open access article under the CC BY license (http://creativecommons.org/licenses/by/4.0/).

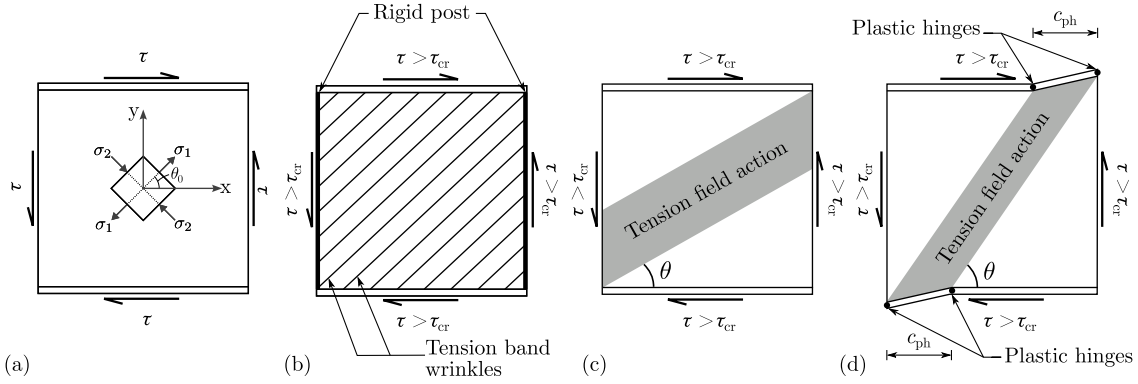


Fig. 1. (a) The pre-buckling stress state of a girder web under shear; the post-buckling tension field action as considered by (b) Wagner [2], (c) Basler [3] and (d) Porter et al. [4] and Höglund [5].

method and the flanges though the formation of a plastic mechanism, as two separate and distinct contributions to the cross-section shear resistance. Yet, Johansson et al. [13] discussed how the predictions of EN 1993-1-5 were calibrated to experimental results on I-section girders, where the contribution of the web and the flange could not readily be separated. Furthermore, the distance at which the plastic hinges in the flange form, depicted as c_{ph} in Fig. 1(d), is underestimated when compared with the observed experimental results, since the plastic mechanism in the flanges does not develop freely owing to the additional support provided by the web [13]. It is also suggested in [13] that the flanges contribute directly to the shear resistance; however, such contributions have not been hitherto thoroughly investigated.

Yoo and Lee [14] countered the notion that the flanges and the transverse stiffeners serve as external anchors to the developed tension-field stresses since the additional membrane stresses are self-equilibrating along the panel edges. Instead, they suggested that the flanges and transverse stiffeners primarily contribute to restraining the boundaries of the web panel, demonstrating this theory through numerical studies [15] and laboratory experiments [16]. They showed that increasing the stiffness of the flanges increased the post-buckling strength of the cross-section disproportionately [14–16].

In the existing shear design approach in EN 1993-1-5 [12] the elastic critical buckling stress of the web is determined by considering the plate in isolation with simply-supported boundary conditions and loaded in pure shear. It has been demonstrated in [17,18] that the elastic buckling stress of the full cross-section can be significantly larger than that of the web plate with simply-supported boundary conditions owing to the flexural restraint provided at the boundaries of the web by the flanges.

Scandella et al. [19] reviewed the current design principles related to the structural behaviour of steel-plate girders in shear, suggesting a generalised 3-stage breakdown of the shear response of slender webs in plate girders comprising: (1) a linear elastic pre-buckling stage, (2) a post-buckling stage where noticeable out-of-plane deflections occur, and (3) an advanced post-buckling stage. In stage 2, the diagonal tension-field load path materialises which, in turn, gives rise to the advanced post-buckling stage where the stiffness of the adjoining flanges and stiffeners is engaged as the shear stiffness of the web itself reduces [20]. Augustyn et al. demonstrated that increasing the flange thickness can change the stage 3 response, from one where a peak is observed at the end of stage 2, to one where strain hardening dominates the response, whereby the resistance continues to increase in stage 3 [20,21].

In the current article, the discussed flange contribution to the ultimate shear resistance of I-sections is explored in detail, following the methodology illustrated in Fig. 2. The presented study is conducted using the finite element (FE) models outlined in Fig. 2, which are developed and analysed within the commercial software package Abaqus [22]. First, the FE model is validated against published experimental results; this is followed by a wider parametric study to investigate the influence of the key geometric parameters on the shear resistance of I-section girders. From this model, the direct through-thickness shear resistance of the flanges is evaluated and quantified. The subsequent study implements the 'isolated panel' model to explore the hypothesis that the simply-supported web in isolation (i.e. without any flanges) can develop the post-buckling tension-field action, as observed in [14,15]. The flange contribution to the enhanced shear resistance of the web is then evaluated by comparing the results of the 'isolated panel' model with those of the I-section 'segment' model loaded in pure shear. The influence of the flanges on the critical buckling stress, presented in [18], is further demonstrated, alongside an analysis of the flange influence on the post-buckling resistance of the web. Hence, rather than considering this flange influence through the development of a plastic-hinge, a new approach for determining the shear resistance of I-sections is proposed, along with corresponding formulae. The results correlate well with the FE models; statistical analyses on the proposed formulae are conducted to evaluate their reliability in line with the Eurocode design recommendations [23]. It is found that the proposed expressions consistently predict the ultimate shear resistance with more accuracy than the EN 1993-1-5 code predictions, as presented in Section 5.4. Finally, a worked example is provided to demonstrate the application of the proposed expressions.

2. FE model of I-section girder test setup

The current section presents the modelling parameters, mesh and boundary conditions for an FE model of a complete I-section plate girder subjected to a point load at mid-span. The design expressions presented in EN 1993-1-5 [12] are calibrated with respect to the results from experimental research conducted on similar girders [13,24]; thus, by validating the FE model with published experimental results, a subsequent parametric study can then explore further the influence of the key geometric parameters on the shear resistance of the I-section.

2.1. Geometry, loading and boundary conditions

A parametric model of the full girder is developed, where the loading and boundary conditions closely match typical experimental setups, as depicted in Fig. 3, comprising a simply-supported I-section girder of span length L loaded with a concentrated load P applied at midspan. A load-controlled analysis is modelled in FE, where the load is specified as distributed point loads along each node located at the intersection of the top flange and the midspan stiffener; this is done to present a more realistic engineering loading scenario. The bending moment and shear force distributions for the setup, depicted in Fig. 3, indicate how the web panels on either side of the point load

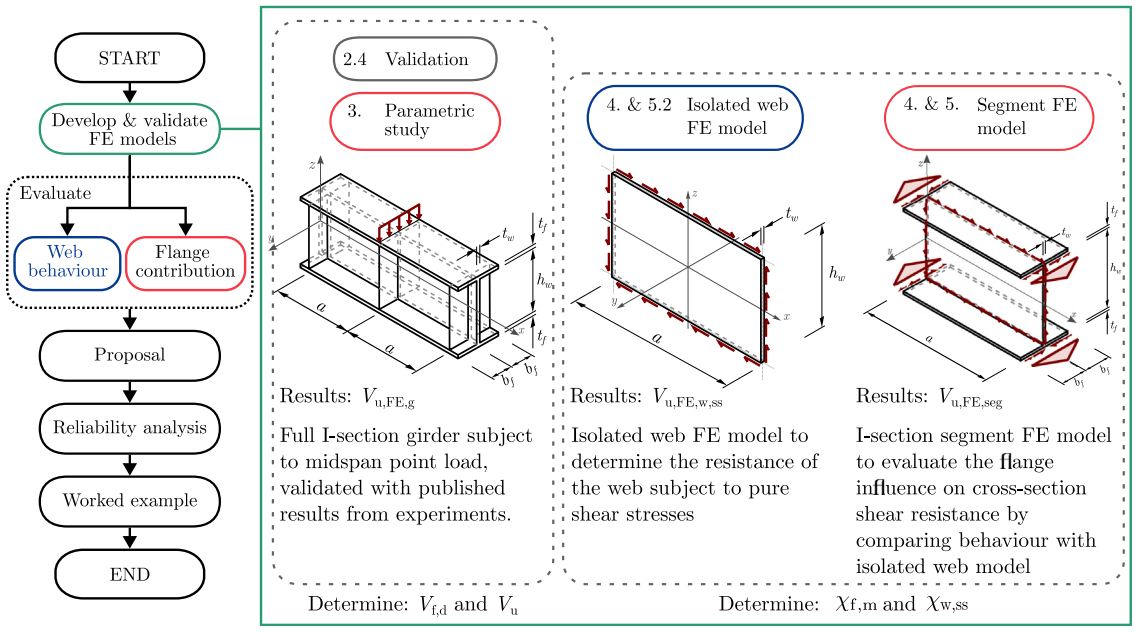


Fig. 2. Flowchart of the analysis methodology and description of the FE models developed to investigate the response of I-sections under shear.

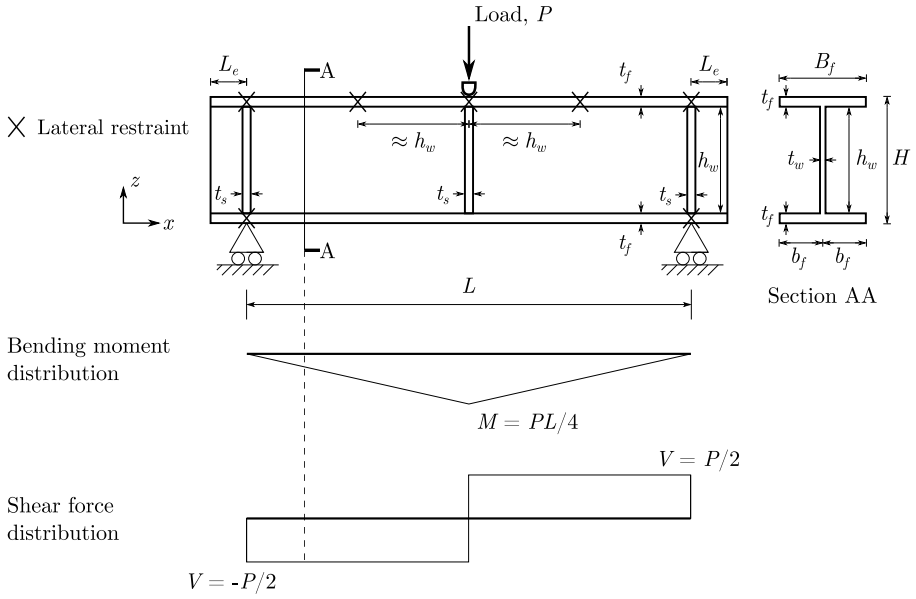


Fig. 3. General experimental layout of an I-section girder of span L subjected to a point load P at midspan. Lateral restraints are located at points marked with a '×' at locations described in the text. The shear force distribution, showing the maximum shear force V, applied to each panel, is equal to $P/2$.

are subjected to a constant shear load of magnitude $V = P/2$, and a coexistent bending moment M that increases linearly to a peak value of $M = PL/4$ at mid-span. The girders extend by length L_e beyond the supports to facilitate testing; these extensions have been replicated in the FE model, as shown in Fig. 3. In the FE models, the flange reference surfaces are modelled at the inner face of the web–flange junction, with the flange thickness offset in the appropriate directions such that the physical web height can be modelled directly and the overall section dimensions match those depicted in Fig. 3.

Transverse stiffeners of thickness t_s and width extending to the flange tips are included at the supports and beneath the load application point to reduce stress concentrations by spreading the load throughout the cross-section. The specified values of t_s are used when available in the descriptions of the tests; elsewhere, the expression:

$$t_s = \max\left\{\frac{3t_w\tau_{y,w}h_w}{2\sigma_{y,w}B_f}, t_f, 2t_w\right\}, \quad (1)$$

is implemented to ensure sufficient strength and rigidity of the transverse stiffener, where $\sigma_{y,w}$ and $\tau_{y,w}$ are respectively the direct yield stress and shear yield stress of the web material. All the girders have been modelled with non-rigid end posts, implying end-plates are not included at the extremities of the overhang L_e. The consideration of rigid end posts on the shear resistance of I-sections is thus not considered in the present study and shall be addressed in future work.

To avoid premature failure of the beam under bending through lateral torsional buckling (LTB), lateral restraints are introduced, indicated with the symbol '×' in Fig. 3, at the intersection of the web and:

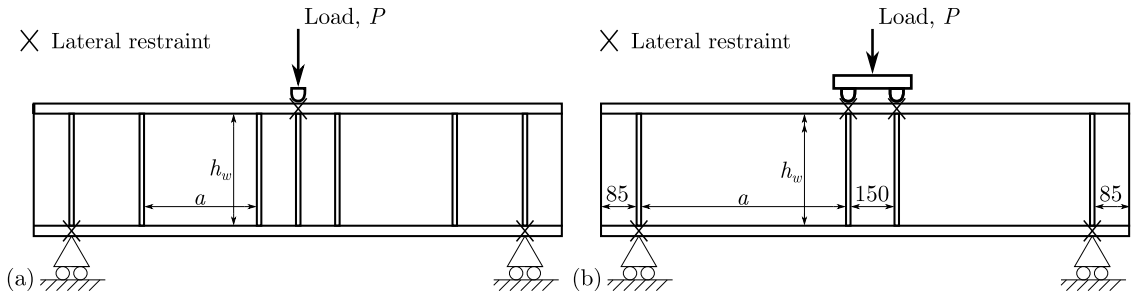


Fig. 4. Depiction of the experimental setups by (a) Lee and Yoo [7] and (b) Kwon and Ryu [8], that are replicated within the FE models for the validation study. Dimensions in mm, lateral restraints are located at points marked with a '×'.

- the lower flange at the supports,
- the top flange above the supports,
- the top and bottom flanges at midspan, i.e. at the point of load application, and
- for girders with the web panel aspect ratio $a/h_w > 1$, additional lateral restraints are placed at the web-to-top-flange junctions at intervals measuring $\approx h_w$.

2.2. Material properties and FE mesh parameters

For an FE model to replicate the experimental response accurately, the specified material description must closely match that of the test material. Typically, tensile coupon tests are conducted on samples from the test specimen to provide the full stress–strain characteristics for input into the FE simulation [8]. Yun and Gardner [25] developed a 'quad-linear material model' (QLM), which was calibrated against over 500 measured stress–strain curves [25], thereby providing an accurate material model for use in advanced numerical analyses where the full stress–strain curve is not necessarily available. The versatility of the material model lies in its simplicity, since it only requires the specification of the material yield stress σ_y, ultimate tensile stress σ_u and Young's modulus E, which are frequently reported or known to the user. However, in some instances, the ultimate tensile stress may not have been reported in the literature. Gardner and Yun [26] developed relationships between the ultimate tensile stress and yield stress for hot-rolled and cold-rolled steel to cater for these circumstances. The present study is limited to hot-rolled steel; thus, the expression [26]:

$$\frac{\sigma_u}{\sigma_y} = 1 + \left(200/\sigma_y\right)^{1.75}, \tag{2}$$

is used to determine σ_u where it is not specified. The relationship in Eq. (2) is based on a regression analysis of 537 hot-rolled carbon steel coupon tests [26]. The QLM has been implemented throughout the current study wherever the FE models include material nonlinearity.

Following a mesh convergence study, the general-purpose four-noded shell element comprising six degrees of freedom per node with reduced integration (S4R) is selected, and 50 elements are implemented along the height of the web h_w. This element type has been successfully employed in a number of similar previous studies [27–30]. The number of elements across the flange width b_f and along the section length a was varied to maintain a square element aspect ratio [18]. The chosen mesh density provides sufficient accuracy without excessive computational effort.

2.3. Analysis methodology

The analysis is conducted in two stages, starting with a linear bifurcation analysis (LBA) to determine the linear eigenvalues and corresponding eigenmodes, and followed by a geometrically and materially nonlinear analysis with imperfections (GMNIA) using the Riks algorithm [31] as implemented within Abaqus [22]. Imperfections are introduced into the GMNIA by scaling the critical eigenmode from the LBA by an appropriate magnitude [22]. In some instances, the models underwent large deformations with no obvious peak load detected. In such cases, failure was determined using the methodology proposed in [32], where the tangent stiffness of the load–deformation curve is determined, and failure is defined at the point where the tangent stiffness reduces to 1% of the original value. Additionally, the maximum plastic deformation is limited to 5% as recommended in prEN 1993-1-14 [33], to ensure that excessive plastic deformations do not form before the ultimate load is reached in the numerical analysis.

2.4. Validation of FE model

The FE model is validated against results from experiments presented in the literature. Hingnekar and Vyavahare [9] collated a list of published experimental results on plate girders in shear, noting the parameters studied and commenting on the findings of each study. The published experimental results by Lee and Yoo [7], Kwon and Ryu [8] and Gomes et al. [34] have been selected to validate the FE model developed herein. This is owing to the similarity of the experimental setups with the model shown in Fig. 3, and because the experiments were conducted on steel I-sections with non-rigid end posts that failed in a shear-dominated mechanism in the web [7,8,34], thus matching the FE model described in Section 2.1.

The experimental arrangements of [7,8] are depicted in Fig. 4, while the arrangement of [34] is identical to that depicted in Fig. 3. The parametric FE model geometry of Fig. 3 is modified to match the experimental setups shown in Fig. 4 and the experimental material properties, as reported in [7,8,34], are utilised within the QLM model for the validation study. The lateral restraints for the validation models are indicated in Figs. 3–4. Initial imperfections affine to the first eigenmode extracted from an LBA of the FE model are also implemented. However, the imperfection magnitudes of the test specimens were not measured in [7,8,34] and therefore an imperfection sensitivity study was conducted to determine the appropriate imperfection magnitude to predict the ultimate shear resistance and mechanism in the FE models accurately. The results of the imperfection sensitivity study are presented in Fig. 5, where very little sensitivity to the initial imperfection magnitude is shown, as also found by other researchers [35]. This imperfection study was conducted for all experimental validation studies, and it was determined that an imperfection magnitude of $h_w/100$ is necessary to reliably reproduce the experimental load–deflection response and predict the ultimate load in [8], while an imperfection magnitude of $h_w/250$ is sufficient to reproduce the results in [7,34] reliably. The geometric and material properties from [7,8,34] are reproduced in Table 1, together with the maximum experimental shear force, V_{exp}, and the predicted maximum shear force from the current FE validation study, $V_{u,FE,g}$. Evidently, the FE model can generally predict the ultimate failure loads with good accuracy. The discrepancies between the FE model results and the experimental results are presently attributed to the fact that the FE model does not include residual stresses, which

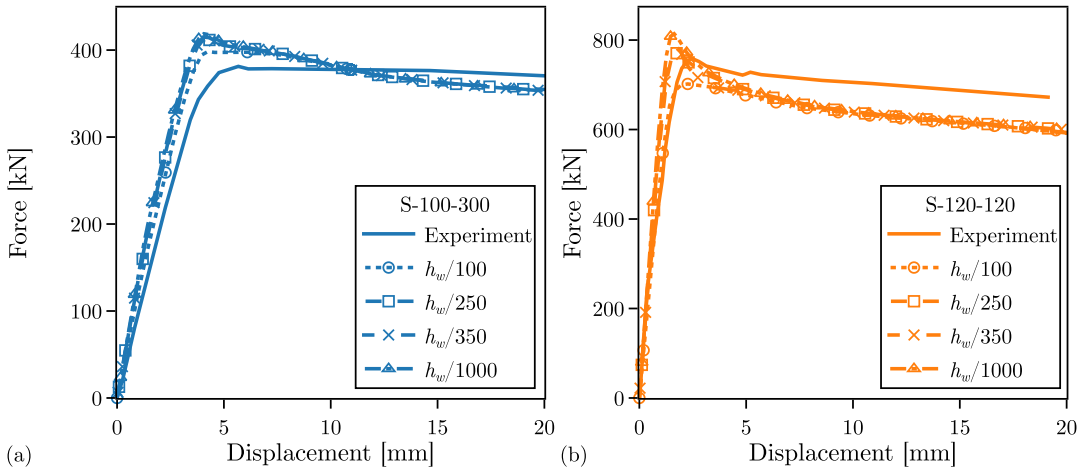


Fig. 5. Imperfection sensitivity study of the FE models replicating the (a) S-100-30 and (b) S-120-120 experiments by Kwon and Ryu [8].

Table 1
Material properties and results of experimental analyses, together with a comparison of the results from the FE model.

Ref	Specimen	a [mm]	h_w [mm]	a/h_w	B_f [mm]	t_w [mm]	t_f [mm]	t_s [mm]	t_f/t_w	E [MPa]	$\sigma_{y,w}$ [MPa]	$\sigma_{y,f}$ [MPa]	Imperfection magnitude	V_{exp} [kN]	$V_{u,FE,g}$ [kN]	$\frac{V_{exp}}{V_{u,FE,g}}$
[7]	G1	400	400	1.00	130	4.0	15	6	3.75	204	318.5	303.8	$h_w/250$	282.4	269.3	1.05
	G2	600	600	1.00	200	4.0	10	6	2.50	204	318.5	303.8	$h_w/250$	332.5	334.1	1.00
	G3	600	600	1.00	200	4.0	15	6	3.75	204	318.5	303.8	$h_w/250$	337.4	345.9	0.98
	G4	600	400	1.50	130	4.0	15	6	3.75	204	318.5	303.8	$h_w/250$	268.8	245.3	1.10
	G5	900	600	1.50	200	4.0	10	6	2.50	204	318.5	303.8	$h_w/250$	286.4	292.5	0.98
	G6	900	600	1.50	200	4.0	20	6	5.00	204	318.5	303.8	$h_w/250$	312.8	311.5	1.00
	G7	1200	600	2.00	200	4.0	10	6	2.50	204	285.2	303.8	$h_w/250$	258.9	259.3	1.00
	G8	1200	600	2.00	200	4.0	15	6	3.75	204	285.2	303.8	$h_w/250$	276.5	270.6	1.02
[34]	VT1	900	300	3.00	100	2.0	5	5	2.50	206	274.0	274.0	$h_w/250$	54.8	57.3	0.96
[8]	S-60-120	440	576	0.76	150	4.5	12	12	2.67	200	339.2	374.5	$h_w/100$	448.2	429.9	1.04
	S-60-180	740	576	1.28	150	4.5	12	12	2.67	200	339.2	374.5	$h_w/100$	332.4	362.4	0.92
	S-60-240	1040	576	1.81	150	4.5	12	12	2.67	200	339.2	374.5	$h_w/100$	319.5	337.5	0.95
	S-60-300	1340	576	2.33	150	4.5	12	12	2.67	200	339.2	374.5	$h_w/100$	300.6	323.1	0.93
	S-80-120	440	776	0.57	250	4.5	12	12	2.67	200	339.2	374.5	$h_w/100$	522.6	537.3	0.97
	S-80-180	740	776	0.95	250	4.5	12	12	2.67	200	339.2	374.5	$h_w/100$	424.3	440.8	0.96
	S-80-240	1040	776	1.34	250	4.5	12	12	2.67	200	339.2	374.5	$h_w/100$	365.5	396.2	0.92
	S-80-300	1340	776	1.73	250	4.5	12	12	2.67	200	339.2	374.5	$h_w/100$	336.7	373.8	0.90
	S-100-120	440	976	0.45	250	4.5	12	12	2.67	200	339.2	374.5	$h_w/100$	623.5	632.0	0.99
	S-100-180	740	976	0.76	250	4.5	12	12	2.67	200	339.2	374.5	$h_w/100$	485.8	516.3	0.94
	S-100-240	1040	976	1.07	250	4.5	12	12	2.67	200	339.2	374.5	$h_w/100$	426.5	446.2	0.96
	S-100-300	1340	976	1.37	250	4.5	12	12	2.67	200	339.2	374.5	$h_w/100$	380.2	411.1	0.92
	S-120-120	440	1176	0.37	250	4.5	12	12	2.67	200	339.2	374.5	$h_w/100$	757.7	742.1	1.02
	S-120-180	740	1176	0.63	250	4.5	12	12	2.67	200	339.2	374.5	$h_w/100$	540.0	592.4	0.91
	S-120-240	1040	1176	0.88	250	4.5	12	12	2.67	200	339.2	374.5	$h_w/100$	474.8	500.6	0.95
	S-120-300	1340	1176	1.14	250	4.5	12	12	2.67	200	339.2	374.5	$h_w/100$	433.9	451.9	0.96
															Mean	0.97
															St. dev.	0.05

inevitably arise from the fabrication procedure, and may explain the slightly stronger and stiffer response of the FE models.

Further validation of the FE model is conducted by comparing the equilibrium paths of applied shear load versus deflection from the numerical model and experiments, which are shown in Fig. 6. The response shown in Fig. 6 echoes the discussion above, and shows the FE models to have a slightly stiffer response in general in comparison with the experimental results. However, since the ultimate load is governed by the failure of the web panel in shear, the FE ultimate load prediction closely matches that of the experimental results, as expected. A qualitative assessment of the load–deflection curves inspires further confidence in the FE model, showing comparable responses at each loading stage and in the post-failure region. In Fig. 7, photographs of the failure mode from the experiments in [7,8] are compared with the deformed model from the FE analyses, demonstrating near-identical post-failure mechanisms. The FE models are therefore considered to be sufficiently accurate for the purposes of conducting the parametric study presented herein.

3. Parametric study on I-section girder

A parametric analysis on the girder model with non-rigid end posts, presented in Fig. 3, is conducted to investigate the influence of geometrical parameters on the shear resistance. The geometrical and material properties for the parametric study are presented in Table 2, with h_w fixed to 1000 mm in all cases. Throughout the parametric study, imperfections are introduced into the GMNIA by scaling the critical eigenmode from the LBA by $h_w/250$, in accordance with the recommendations of Annex C of EN 1993-1-5 [12]. Combinations within the range of parameters indicated in Table 2 are further limited to cross-sections with flanges classified as class 1 or 2, determined using the relevant guidance provided in EN 1993-1-1 [36].

3.1. Results of parametric model

Since the girder is loaded in combined shear and bending, as shown in Fig. 3, the results from the parametric study are best interpreted

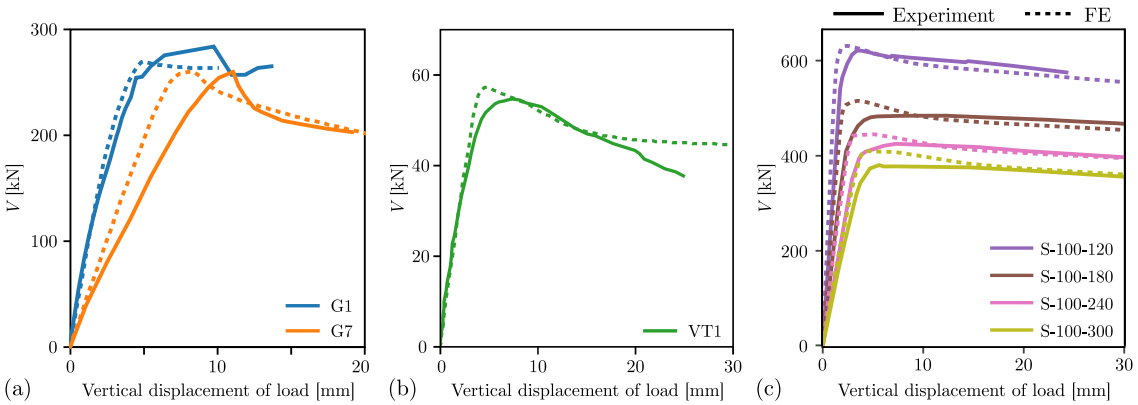


Fig. 6. Comparison of equilibrium paths of applied shear load $V = P/2$ against mid-span vertical displacement between the currently formulated FE models (dashed line) and the published experimental results (solid line) by (a) Lee and Yoo [7], (b) Gomes et al. [34] and (c) Kwon and Ryu [8].

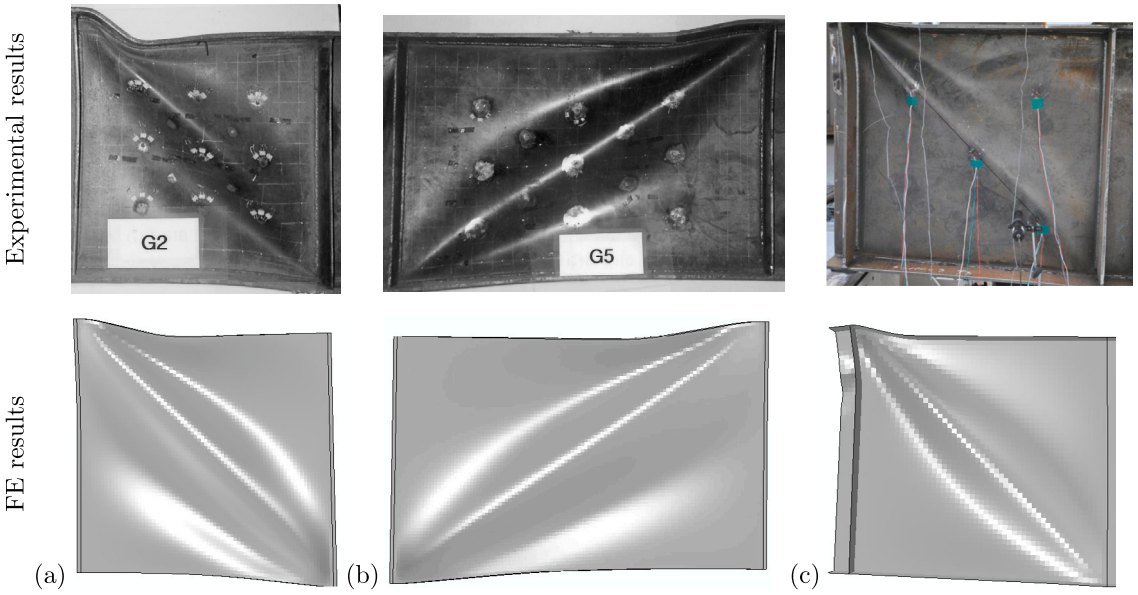


Fig. 7. Comparison of FE and experimental failure mechanisms for girders (a) G2 and (b) G5 from Lee and Yoo [7], and (c) S100-240 from Kwon and Ryu [8].

Table 2
Geometric and material parameters of FE models.

Quantity		Values
Young's Modulus	E	210 kN/mm^2
Poisson's ratio	ν	0.3
Yield stress	$\sigma_{y,w}, \sigma_{y,f}$	355 N/mm^2
Web height	h_w	1000 mm
Web thickness	t_w	$\{6, 8, 10, 12, 20\}$ mm
Web aspect ratio	a/h_w	$\{0.5, 0.6, 0.7, 0.8, 0.9, 1.0, 1.5, 2.0, 3.0, 4.0, 5.0\}$
Flange to web thickness	t_f/t_w	$\{1, 2, 3, 4, 5\}$
Flange width to web height	B_f/h_w	$\{0.2, 0.4, 0.6\}$

on a shear–moment interaction diagram, as plotted in Fig. 8. The black lines in Fig. 8(a) represent the interaction curves for the cross-sections, derived using the relevant clauses in EN 1993-1-5 [12], with the ordinate being normalised by the web buckling resistance $V_{\text{bw,Rd}}$, while the abscissa is normalised by the bending moment resistance of the effective cross-section $M_{\text{c,Rd}}$. The web shear buckling resistance is defined as:

$$V_{\text{bw,Rd}} = \chi_{w,\text{EC3}} \frac{\tau_{y,w} h_w t_w}{\gamma_{M1}}, \tag{3}$$

where $\chi_{w,\text{EC3}}$ is a shear buckling reduction factor based on the end conditions of the girder and γ_{M1} is a partial safety factor employed

Table 3
Shear buckling reduction coefficient $\chi_{w,\text{EC3}}$ for girders as given in EN 1993-1-5 [12].

λ_w	Rigid end-post	Non-rigid end-post
$\lambda_w < 0.83/\eta$	η	η
$0.83/\eta \le \lambda_w < 1.08$	$0.83/\lambda_w$	$0.83/\lambda_w$
$\lambda_w \ge 1.08$	$1.37/(0.7 + \lambda_w)$	$0.83/\lambda_w$

when determining the resistance of members to instability [12,23]. The EN 1993-1-5 [12] values of $\chi_{w,\text{EC3}}$ are given in Table 3, where λ_w is the normalised web slenderness defined as:

$$\lambda_w = \lambda_{\tau,\text{ss}} = \sqrt{\tau_{y,w}/\tau_{cr}}, \tag{4}$$

which is presently also referenced as $\lambda_{\tau,\text{ss}}$ to indicate the slenderness of the simply-supported web panel, while η is a coefficient introduced in EN 1993-1-5 [12] that accounts for the strain hardening region of the material beyond the yield plateau. A value of $\eta = 1.2$ is typically considered for steel grades up to and including S460, with $\eta = 1.0$ being adopted for higher steel grades [12].

The features of a typical interaction curve are depicted in Fig. 8(b). When the coexisting moment applied to the cross-section M_{Ed} is less than $M_{\text{f,Rd}}$, the cross-section resistance is calculated thus [12]:

$$V_{\text{b,Rd,EC3}} = V_{\text{bw,Rd}} + V_{\text{bf,Rd}}, \tag{5}$$

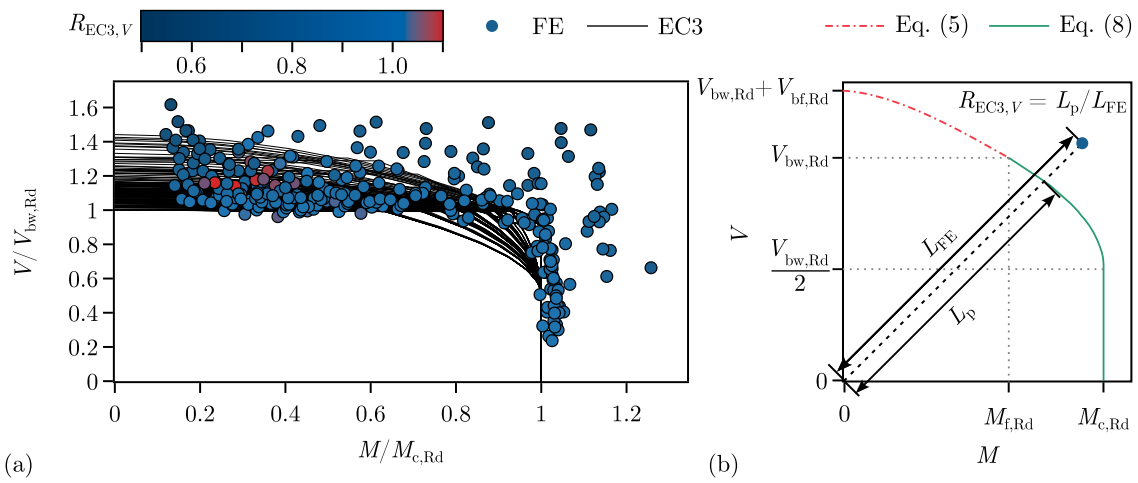


Fig. 8. (a) Interaction diagrams of applied shear force normalised with the shear resistance of the web $V/V_{bw,Rd}$ against applied moment normalised with the effective moment of resistance of the cross-section $M/M_{c,Rd}$; (b) schematic depicting the elements of the interaction curve and the calculation of $R_{EC3,V}$. (For interpretation of the references to colour in this figure legend, the reader is referred to the web version of this article.)

where $V_{bf,Rd}$ is the flange contribution to the shear resistance, which is defined as [12]:

$$V_{bf,Rd} = \frac{B_f t_f^2 \sigma_{y,f}}{c_{ph}\gamma_{M1}}\left[1-\left(\frac{M_{Ed}}{M_{f,Rd}}\right)\right], \tag{6}$$

where $M_{f,Rd}$ is the bending resistance of the flanges alone and c_{ph} is the location of the plastic hinge that is estimated using [12]:

$$c_{ph} = a\left(0.25+\frac{1.6B_f t_f^2\sigma_{y,f}}{t_w h_w^2 \sigma_{y,w}}\right) \tag{7}$$

Otherwise,

$$\frac{M_{Ed}}{M_{pl,Rd}}+\left(1-\frac{M_{f,Rd}}{M_{pl,Rd}}\right)\left(2\frac{V_{Ed}}{V_{bw,Rd}}-1\right)^2 \le 1.0 \qquad \text{for } M_{Ed} \ge M_{f,Rd}, \tag{8}$$

where V_{Ed} is the applied shear force, $M_{pl,Rd}$ is the design plastic bending resistance of the full cross-section.

The interaction curve was established based on the lower bound theorem of plasticity [13], with an added limit to account for the interaction only when $V_{Ed} \ge 0.5V_{bw,Rd}$; this limit was based on empirical evidence from test girders that do not demonstrate any interaction below this load level [13]. Since $M_{pl,Rd}$ is used as the basis for this interaction, regardless of its section classification, a limit on the interaction is imposed such that the applied moment is limited to the elastic or effective cross-section capacity $M_{c,Rd}$ for class 3 and 4 sections, respectively. The prediction ratio $R_{EC3,V}$ of the FE results relative to the calculated resistance of EN 1993-1-5 [12], shown in Eq. (8), is determined for each of the cross-sections in the parametric study using:

$$R_{EC3,V} = L_p/L_{FE}, \tag{9}$$

where L_{FE} and L_p are defined in Fig. 8(b). In Fig. 8(a), the results with $R_{EC3,V} \le 1$ are safe-sided and indicated with blue markers, whereas when $R_{EC3,V} > 1$ the results are depicted with red markers; this approach has been successfully applied in previous studies [18,37]. The FE models perform well compared to the current Eurocode predictions, with only a few points marginally below the design predictions. Furthermore, the results indicate very little interaction between the shear and bending for I-sections, reinforcing the discussion in [13].

In Fig. 9(a), the ultimate shear resistance of the cross-section normalised with the shear yield resistance of the web V_y, which is defined as:

$$V_y = \tau_{y,w} t_w h_w, \tag{10}$$

is plotted as a function of the slenderness of the cross-section $\lambda_{\tau,cs}$, which is defined thus:

$$\lambda_{\tau,cs} = \sqrt{\tau_y/\tau_{cr,cs}}. \tag{11}$$

The cross-section slenderness $\lambda_{\tau,cs}$ is calculated using the formulae and methodology presented in [18]. Despite the results in Fig. 8 showing seemingly little interaction between shear and bending, the results in Fig. 9(a) are limited to a subset of the sections where $M_{Ed} < M_{f,Rd}$ to isolate cross-sections loaded predominantly in shear. The results, plotted as red circles in Fig. 9(a), indicate the total shear force resisted by the cross-section as predicted from FE, $V_{u,FE,g}$, which is the value typically measured and reported from physical tests [9,24], as shown in Table 1. Despite having modelled girders with non-rigid end posts, the results for $V_{u,FE,g}$ presented in Fig. 9(a) are shown to be stronger than the predictions for girders with rigid end posts according to EN 1993-1-5 [12], which are plotted as the dashed black lines. The reasons for this increased resistance are explored further, founded on the discussion presented in Section 1.

3.2. Direct flange contribution in shear

The direct contribution of the flanges to the shear resistance is studied by analysing the results of the girders modelled in FE by determining the relative contribution of the constituent plate elements. This is achieved by extracting the stresses through the cross-section of the FE models, determined from a free-body cut taken at a distance of $x = a/2$ from the support. The value of $x = a/2$ was selected following an initial study where it was concluded that the web contribution in shear is at its largest at $x = a/2$, and hence it would be conservative to consider the flange contribution at this location. A typical stress distribution through a free-body of the I-section is depicted in Fig. 10, showing the parabolic shear stress distribution in the elastic range down the height of the web and the relatively small contributions from the flanges. The inset diagram in Fig. 10 details the individual through-thickness shear stress distribution in the flanges, alongside the element-local coordinate systems, where subscripts 'f' and 'w' respectively refer to the flange and web element orientations; knowledge of the element-local orientation ensures that the correct stresses are extracted from the FE results in the subsequent analyses. For each of the girders analysed, the contribution of the constituent flanges and web can be obtained by integrating the stresses depicted over the entire cross-section. Thus, the web contribution $V_{FE,w}$ is established by integrating $\sigma_{12,w}$ over the web thickness t_w and height h_w, while the flange contribution $V_{FE,f,d}$ is established by integrating $\sigma_{13,f}$ over the flange thickness t_f and

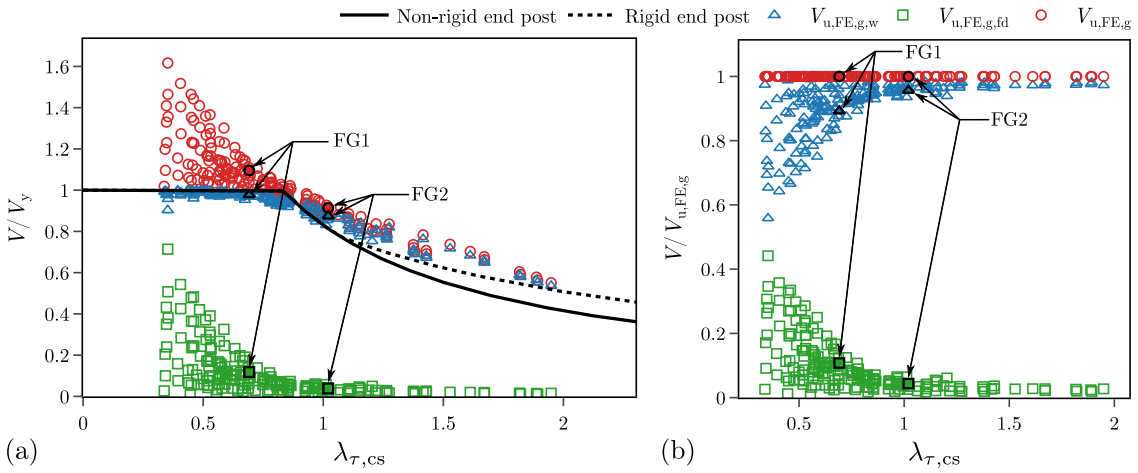


Fig. 9. (a) Normalised shear resistance V/V_y versus $\lambda_{\tau,cs}$; circles indicate total FE resistance $V_{u,FE,g}$, triangles indicate web contribution to the resistance $V_{u,FE,g,w}$ and squares indicate direct contribution of the flange in shear $V_{u,FE,g,fd}$, lines represent design curves from EN 1993-1-5 [12] for non-rigid (solid line) and rigid (dashed line) end posts, and arrows indicate the results for FG1 and FG2; (b) component contributions $V_{u,FE,g,w}$ and $V_{u,FE,g,fd}$ relative to $V_{u,FE,g}$ versus $\lambda_{\tau,cs}$.

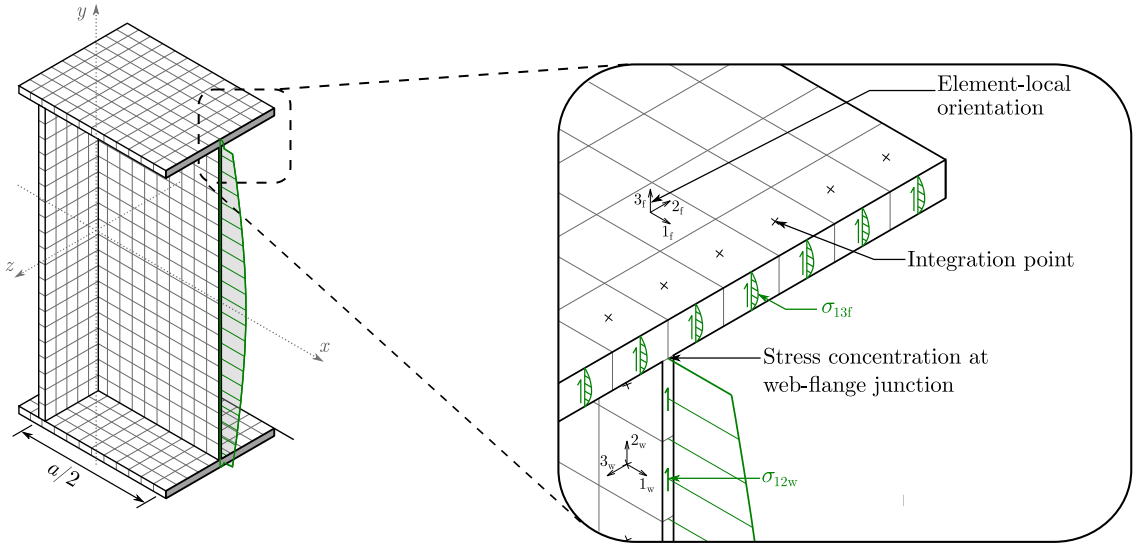


Fig. 10. Schematic of the shear stress distribution within the cross-section in the elastic range, indicating the stresses extracted from Abaqus at $x = a/2$, to determine the flange direct contribution in shear.

across the flange width B_f of each flange. For the element orientations depicted in Fig. 10, this is easily obtained in Abaqus by extracting the section force resultants 'SF3' from the web and 'SF4' from the flanges at each element integration point, which, according to the Abaqus user manual, are the results of the stresses integrated throughout the thickness of the element per unit length of the element [22]. The total shear force is obtained by multiplying the extracted section forces by the respective element widths. For the S4R element, the integration point is located at the element centroid, as depicted in Fig. 10. The accuracy of the approach is ensured by comparing the sum of the forces extracted from the free-body, using the procedure described, with the reaction force at the ends of the girders; the forces should be equal for the girder since the shear force distribution is constant along the panel length a, as shown in Fig. 3.

The procedure is demonstrated for sample girders FG1 and FG2, which are selected from the parametric results as indicated in Fig. 9(a). The properties and results of FG1 and FG2 are depicted in Fig. 11. The equilibrium paths of applied shear force with vertical displacement of the point load are depicted in Fig. 11(b), which demonstrates a clear linear-elastic response from the onset of loading that eventually drops in stiffness, until the peak load is reached. Beyond the peak load, a small drop in resistance is observed for both girders; however, most of the strength is maintained. FG1 has an aspect ratio of $a/h_w = 1$, thus a free-body is taken at $x = 500$ mm and the resulting stresses through the cross-section are depicted in Fig. 11(c) when $V = 1411$ kN, i.e. at an arbitrary load step during the linear-elastic response of the girder. The stress distribution generally follows the typical shear stress distribution derived from elastic beam theory, particularly highlighting the parabolic distribution of the shear stresses throughout the web alongside the stress peak at the web-to-flange junction. The asymmetry of the values of the stresses between the top and bottom flange and the left and right-hand side of the section is attributed to the inclusion of geometric imperfections in the FE models. The total shear force extracted matches the reaction force at the support, thus confirming the accuracy of the approach. The stress distribution at the ultimate limit state, i.e. at $V = 3431$ kN $= V_{u,FE,g}$, is depicted in Fig. 11(d), where plasticity is observed to dominate the response throughout the cross-section. The web stress resultant at yield is obtained by multiplying the shear yield stress and the web thickness, thus $\tau_{y,w} \times t_w = 204.95 \times 15$ mm $= 3074$ N/mm. Therefore, the web has yielded throughout almost the entire depth of the cross-section, as shown in Fig. 11(d), a feature which would be expected from a relatively stocky girder with $\lambda_{\tau,cs} =$

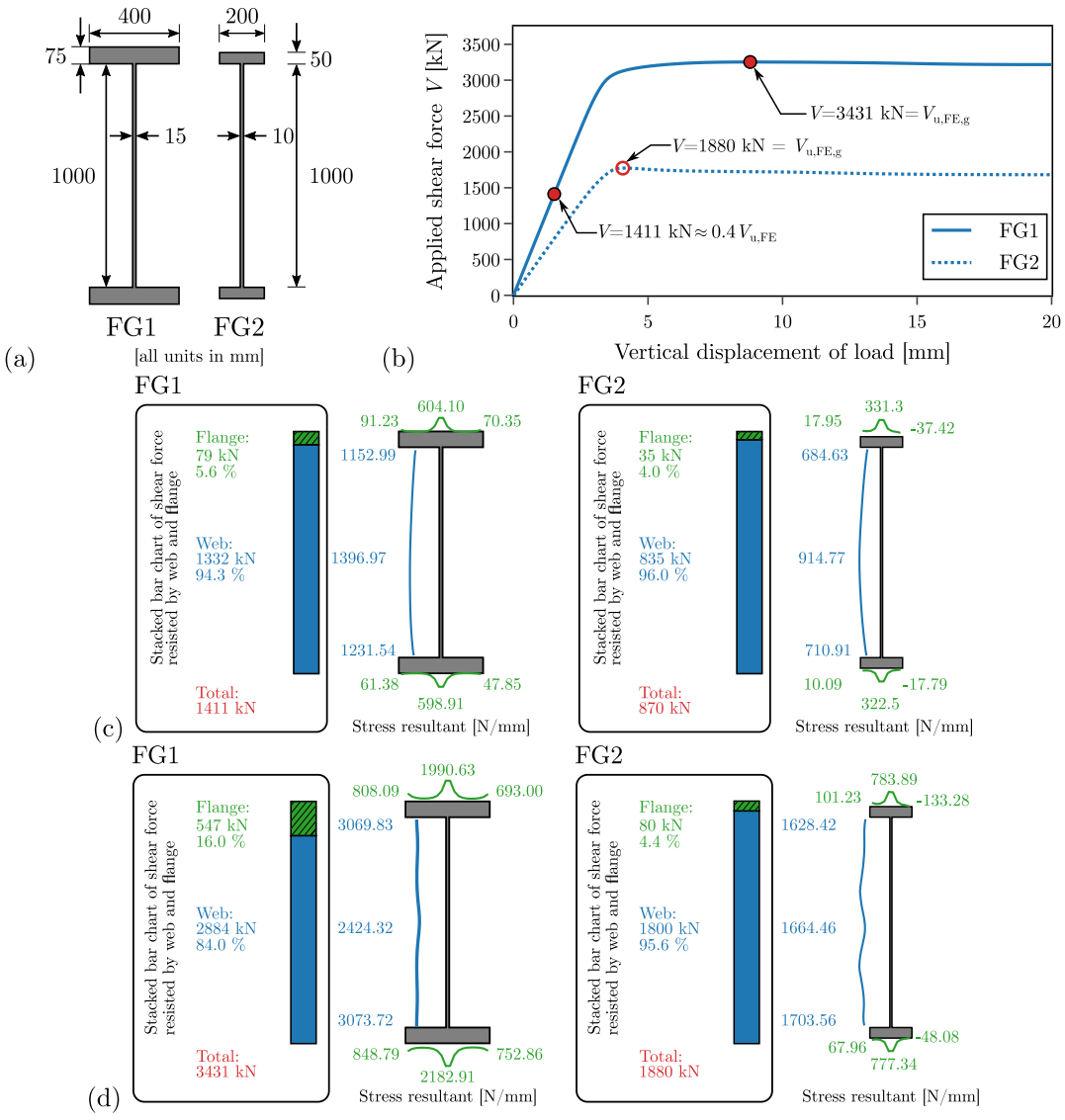


Fig. 11. (a) Cross-section geometry and parameters of FG1 and FG2 with $a/h_w = 1$; (b) equilibrium paths of applied shear force versus vertical displacement of point load; stresses through free-body of FG1 and FG2 at $x = a/2$ when $V/V_{u,FE,g}$ is: (c) approximately 0.4 and (d) 1.

0.69. For FG2, the web stress resultant at yield is $\tau_{y,w} \times t_w = 204.95 \times 10$ mm $= 2050$ N/mm, thus from Fig. 11(d) it follows that the web has not yielded. This result is expected since FG2 is relatively slender with $\lambda_{\tau,cs} = 1.02$. It is noted, however, that such stress distributions are not typical to all the girders in the parametric study, especially those where high deformations and strain hardening generally result in more complex stress distributions.

The relative contribution of the flange and web to the overall shear resistance of the cross-section is evaluated and presented alongside the stress distributions through the cross-section in Fig. 11(c)–(d). It is noted that in FG1, there is a demonstrable increase in the flange contribution as the applied load increases. In the initial stages, during the linear elastic region, the flange contributed approximately 5% of the total shear force resisted by the section. This contribution increased to approximately 16% of the overall shear force at the ultimate limit state, which is attributed to the plastic redistribution of shear stress [19]. For FG2, the flange proportions relative to the web do not allow for an increased contribution to the shear resistance in the post-buckling phase [19–21], as demonstrated in Fig. 11(c)–(d).

The procedure detailed herein for FG1 is repeated for all the girders in the parametric study, and the web and flange contributions derived from the free-body analysis of each cross-section are depicted in Fig. 9(a) with triangles and squares, respectively. The relative contribution of the web and the flange to the overall shear resistance is determined by normalising the results with the total resistance, which is plotted in Fig. 9(b). The flange contribution is noted to be at its greatest when the cross-section slenderness $\lambda_{\tau,cs}$ is low (i.e. stocky webs), with its influence diminishing as $\lambda_{\tau,cs}$ increases. A detailed study of the parameters influencing the direct stress contribution, alongside formulae for predicting the shear resistance, is presented in Section 5.1.

4. Flange influence on web resistance in shear

The current section examines the influence of the flange on the buckling and post-buckling resistance of the web of an I-section loaded in shear. Two additional FE models, depicted in Fig. 12, are developed from the FE model presented in Section 2 to investigate this influence. The ‘isolated panel’ model, presented in Fig. 12(a), is developed to study the web plate of the I-section in isolation, i.e. without the flanges present. The plate is loaded in pure shear, the force of which is distributed along the edges as indicated, and modelled with simply supported boundary conditions, as per the assumptions of Höglund’s rotated stress field model. The ‘segment’ model, depicted in Fig. 12(b), is then utilised to examine the response of the web panel within an

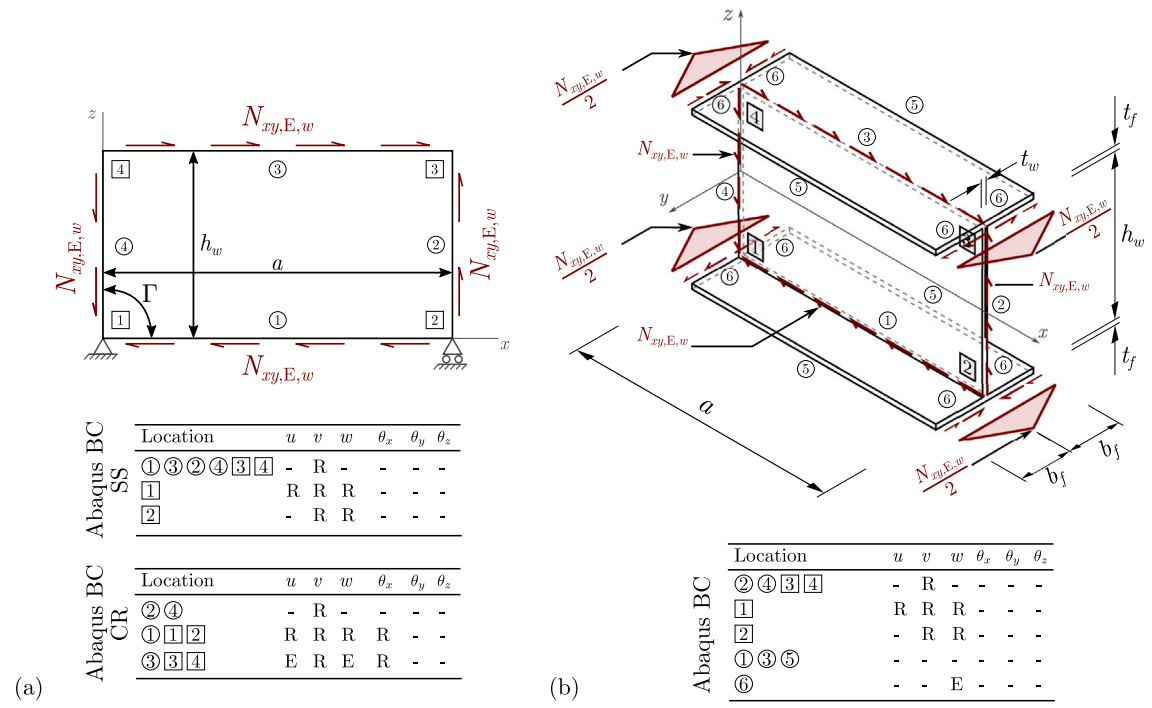


Fig. 12. Geometry and nomenclature of FE model for an isolated flat (a) web panel and (b) I-section segment subject to shear stress. Numbers in circles and squares represent labels assigned edges and corners, respectively. Labels '-' and 'R' indicate free and restrained degrees of freedom, while 'E' represents an equation constraint.

I-section, i.e. accounting for the presence and influence of the flanges. The scope of the current study is limited to the behaviour of I-section girders with non-rigid end posts. Thus the transverse stiffeners and the panel extensions beyond the stiffener boundary are not modelled in the 'segment model' to avoid their influence on the web response. The influence of the end post rigidity will be considered in future work by the authors. The 'segment' model is also loaded in pure shear in isolation, i.e. without any additional direct bending stresses, enabling a direct comparison of the results with those from the 'isolated panel' model. An LBA of the same models was implemented in [18] to determine the elastic buckling stress of I-sections in shear. In the current article, a GMNIA of the models is implemented to determine the post-buckling behaviour under shear.

4.1. FE modelling parameters

The geometrical and material parameters adopted in the present study are the same as presented in Table 2. The four-noded plane stress element with reduced integration and six degrees of freedom per node (S4R) available in the Abaqus library is implemented presently. Both the 'segment' and 'isolated panel' models were meshed with 50 elements along the height of the web h_w, with the number of elements across the flange and along the length of the section varied such that a square element aspect ratio was maintained [18]. The analysis is again conducted in two stages, starting with an LBA such that the critical eigenmode can be implemented as an imperfection seed in a subsequent GMNIA. An imperfection magnitude of $h_w/250$ is employed throughout, such that consistent comparisons with the results from Section 3.1 may be achieved.

The loading and boundary conditions (BCs) for all cases are depicted in Fig. 12, with edges enumerated and encircled, corner nodes enumerated and boxed, while the tables indicate free and restrained boundary conditions with values of '-' and 'R' respectively. The 'isolated panel' models are designed to capture the theoretical upper-bound and lower-bound restraint that the flange may provide, considering both membrane and flexural boundary conditions as discussed by Williams and Aalami [38]. Therefore, for the isolated panel in Fig. 12(a), the boundary condition of θ_x on ① and ③ changes between '-' and 'R' depending on whether the edges are simply-supported (SS) or rotationally clamped (C). The membrane BC of the isolated panel is unrestrained using the parameters specified in Fig. 12(a). A restrained edge (R) is specified by introducing **Pin* multi-point constraints (MPC) in Abaqus, where the translational degrees of freedom of the secondary nodes along an edge are constrained to those of the primary node; in this case, the primary node is the corner node, and the secondary nodes are the intermediate nodes along the edge of the plate. For the 'segment' model in Fig. 12(b), the boundary conditions are such that the flexural and membrane restraints along edges ① and ③ are provided by the flanges, and therefore no boundary conditions are specified on these edges. An **Equation* constraint is applied to the nodes along the supported flange edge, constraining their z-direction deflections to be equal to the deflections of the node at the respective web to flange junction. This provides a theoretical lower-bound (i.e. simply-supported) boundary condition for the stiffeners, which will be considered in detail in future work. It has been shown in [18] that simplifying the parabolic distribution of the shear stresses along the depth of the web to a state of pure shear stress results in negligible differences compared with a model that explicitly includes the parabolic distribution; the assumption of a uniform shear stress distribution is therefore maintained presently.

4.2. Results and comparison

The results of the 'isolated panel' and 'segment' models are first evaluated in Fig. 13 by comparing the equilibrium paths of the FE response with typical results from the parametric study. The applied shear stress τ is normalised by the yield stress in shear $\tau_{y,w}$ and plotted on the ordinate, while the change in angle of the web panel Γ is plotted on the abscissa, capturing the global response of the web under shear load. The results have been selected to sample the behaviour across the parametric range explored presently, particularly those with different slendernesses, aspect ratios and flange widths. In Fig. 13, the solid lines represent the results of the 'isolated panel' model with simply-supported (SS) boundary conditions and the dashed lines with crosses

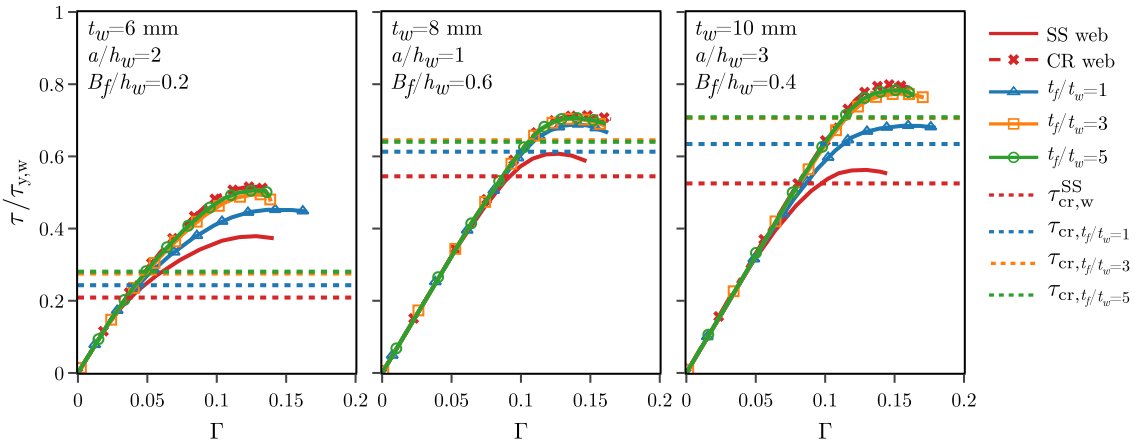


Fig. 13. Equilibrium paths $\tau/\tau_{y,w}$ vs change in shear angle Γ (in radians) for plates with t_w, t_f/t_w, and B_f/h_w as indicated. The isolated model results are depicted with solid lines without markers for simply-supported (SS) boundary conditions, and the lines with cross-markers for clamped-restrained (CR) boundary conditions; the segment model results when t_f/t_w is 1,3 and 5 are represented by the triangle, square and circle markers, respectively. The elastic critical buckling stress of the respective models is depicted using the dashed horizontal lines, as indicated in the legend. (For interpretation of the references to colour in this figure legend, the reader is referred to the web version of this article.)

represent the results with clamped-restrained (CR) edges. Clamped-restrained boundary conditions imply that edges ① and ③ in the 'isolated panel' model are enforced to remain straight, i.e. with an infinite membrane stiffness, and the rotational restraint is clamped, i.e. no rotation is allowed. Thus, the SS and CR results respectively represent the lower and upper bounds of the restraint that the flanges could reasonably provide to the web. The results of the segment model, with varying t_f/t_w ratios, are superimposed onto the same plots in Fig. 13 to assess the influence of the flange. The stiffness response for all the models is identical from the onset of loading, where elastic stresses dominate the response, thus demonstrating that the proposed methodology and FE models are viable for deducing the influence of the flanges on the web.

In Section 1, it was proposed that the flanges stiffen the web along the adjoined edges by (1) restraining the rotation of the plate and (2) restraining the in-plane membrane deformations. The increased rotational restraint results in an increased elastic critical shear buckling stress for the cross-section, which was studied in detail in [18]. The elastic critical shear buckling stress, calculated in accordance with the results in [18], is plotted for each model with dashed horizontal lines in Fig. 13, where the colours correspond to the buckling stress of the simply-supported web $\tau_{cr,w}^{SS}$ and the entire cross-section $\tau_{cr,cs}$ as t_f/t_w increases, as indicated in the legend. In such plots, buckling is manifest when the load–deflection response deviates from the fundamental (initially linear) path. Such deviations are noted to commence just before the predicted elastic critical buckling stress for the cross-section has been reached. This early deviation is attributed to the initial geometric imperfection introduced within the FE model. Nevertheless, the sequence in which each model deviates from the fundamental path is in the order of increasing rotational stiffness, i.e. the SS web buckles first, followed by the segment models with increasing t_f/t_w and finally the CR web, all within a small margin of the predicted critical buckling stress. Thus, the equilibrium paths further verify the accuracy of the predicted elastic critical buckling stress using the methodology established in [18] for shear stresses and [39] for direct stresses. The influence of the flanges on the buckling stress is further demonstrated in Fig. 14. First, the normalised shear resistances $V_{u,FE,seg}/V_y$ are plotted against the web slenderness values determined using $\lambda_{\tau,ss}$, defined in Eq. (4), using black circles. Next, the same $V_{u,FE,seg}/V_y$ ratios are plotted against the cross-section slenderness values $\lambda_{\tau,cs}$, defined in Eq. (11), using red crosses, the results of which are superimposed on the same plot in Fig. 14. The presence of the flanges is noted to increase the elastic critical buckling stress of the section, thus causing the cross-section slenderness $\lambda_{\tau,cs}$ to decrease; this effect is visible as a 'shift' in the plotted results towards the left without altering the value of the results on the ordinate, as shown in Fig. 14. The accurate prediction of the cross-section slenderness reduces the spread of the results, as seen in Fig. 14.

The membrane restraint provided by the flanges to the web influences the post-buckling response of the web, i.e. this influence is manifest later in the load–deflection response of the web. In Fig. 13, this is observed by the increased ultimate load-carrying capacity of the segment models compared with the SS web, alongside a stiffer post-buckling response. The membrane restraint increases with increasing flange thickness, as shown in Fig. 13. Finally, it is also noted that the SS and CR models are evidently lower and upper bounds respectively to the response of the 'segment' model with varying t_f/t_w, further validating the hypothesised flange restraint.

For each of the results in the parametric study, the flange membrane contribution $V_{FE,f,m}$ to the shear resistance is evaluated using the expression:

$$V_{FE,f,m} = V_{u,FE,seg} - V_{u,FE,w,ss} - V_{u,FE,seg,fd}, \tag{12}$$

where $V_{u,FE,seg}$ is the ultimate shear resistance of the segment model under consideration, $V_{u,FE,seg,fd}$ is the direct contribution of the flanges in shear that is extracted from the FE results using the methodology described in Section 3.1, and $V_{w,ss}$ is the ultimate shear resistance of the isolated SS web plate with corresponding thickness and aspect ratio. This procedure is depicted schematically in Fig. 15, where the shaded area represents $V_{FE,f,m}$, and the results of the procedure applied to the parametric study are plotted in Fig. 16(a). Since the segment models are loaded in pure shear in isolation, the direct contribution of the flanges in shear is shown to be negligibly small — generally contributing less than 1% of $V_{u,FE,seg}$. Meanwhile, the flange membrane contribution is noted to be negligibly small for sections with stocky webs, and the relative contribution to the ultimate resistance of the cross-section increases with slenderness. The relative contributions of each component to the total resistance $V_{u,FE,seg}$ are best observed in Fig. 16(b), where the results are normalised by $V_{u,FE,seg}$. The direct shear contribution $V_{u,FE,seg,fd}$ is evidently negligible. In contrast, $V_{f,m,FE}$ has a greater influence on the load-carrying capacity when the slenderness of the cross-section is high.

5. Predicting the ultimate shear resistance of an I-section

In Sections 3–4, the influence of the flanges on the web shear buckling resistance was demonstrated, showing how the flanges contribute directly, via through-thickness shear stresses, and indirectly by restraining the web panel boundaries, both rotationally and in-plane.

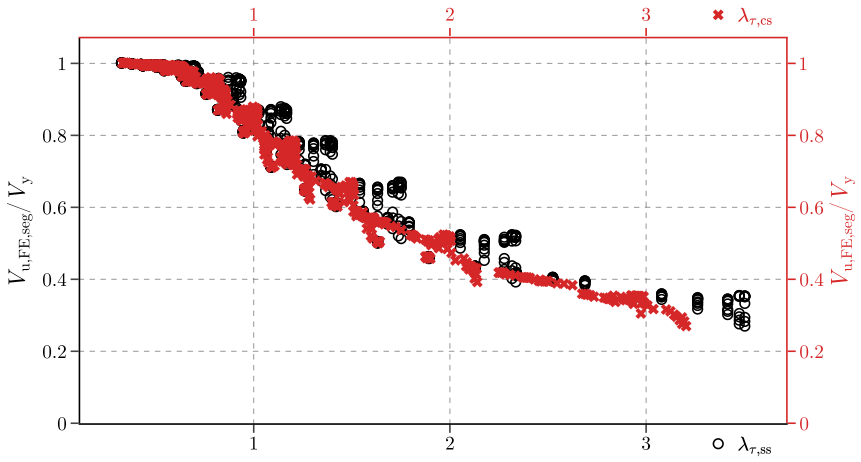


Fig. 14. Normalised ultimate shear resistance $V_{u,FE,seg}/V_y$ versus λ_τ; the circles represent the results normalised with $\lambda_{\tau,ss}$ and the crosses represent the results normalised with $\lambda_{\tau,cs}$.

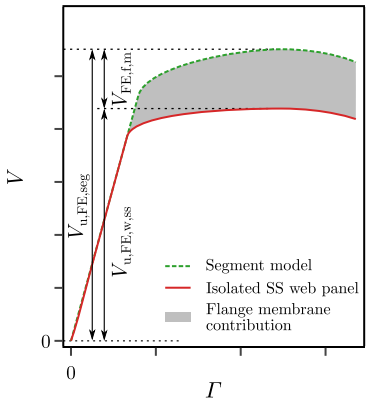


Fig. 15. Schematic depicting the calculation of the membrane resistance from the 'segment' and 'isolated panel' models.

These three components, together with the web contribution, form the basis of the proposed revised shear resistance model $V_{b,prop}$, which is presented thus:

$$V_{b,prop} = V_{b,w,prop} + V_{f,d,prop}, \tag{13}$$

where $V_{b,prop}$ is the predicted shear resistance of the cross-section, $V_{f,d,prop}$ is the direct contribution of the flanges in shear and $V_{b,w,prop}$ is the web shear buckling resistance, which is defined as:

$$\begin{aligned} V_{b,w,prop} &= V_{b,w,ss,prop} + V_{b,f,m,prop}, \\ &= \chi_{w,prop} V_y + \chi_{f,m,prop} V_y, \\ &= \left(\chi_{w,ss,prop} + \chi_{f,m,prop}\right) V_y \qquad \text{for } \left(\chi_{w,ss,prop} + \chi_{f,m,prop}\right) \le 1. \end{aligned} \tag{14}$$

The expression for $V_{b,w,prop}$ is a function of $\chi_{w,ss,prop}$ which is the shear buckling reduction factor for the web alone considering simply-supported boundary conditions, and $\chi_{f,m,prop}$, which represents the contribution to shear resistance of the web due to membrane action provided by the flanges.

Each component of the proposed Eqs. (13)–(14) are presented in further detail in the current section, demonstrating the parameters that influence the resistance alongside formulae to predict the contributions indicated. A statistical analysis follows, which is conducted as per the guidance provided in EN 1990 [23], to demonstrate the reliability of the proposed functions for use in practical design.

5.1. Predicting the direct flange contribution $V_{f,d,prop}$

The data from the parametric study in Section 3.1 is analysed to determine an appropriate prediction model for the direct contribution of the flanges in shear. In Fig. 10, the stress distribution over the flange width was shown to vary as the load applied to the cross-section increased. To explore this influence further, the through-thickness shear stress distribution across the flange width at the ultimate load level is plotted in Fig. 17 for the cross-sections when t_w is (a) 10 mm and (b) 20 mm, and are separated into different plots with $B_f/h_w = 0.2$ and 0.4 as indicated. From Fig. 17, it is observed that the peak direct shear stress distribution across the flange width decreases with decreasing web thickness. Meanwhile, the stress distribution is more uniform across the width of the flange with reducing B_f/h_w. On the basis of these observations, a coefficient $\beta_{f,d}$, which represents a reduction in the effective shear area of the flanges in the I-section that contributes to the shear resistance is established:

$$V_{f,d,prop} = \beta_{f,d} \tau_{y,f} A_f \left[1 - \left(\frac{M_{Ed}}{M_{f,Rd}}\right)^2\right], \tag{15}$$

where A_f is the total area of the flanges in the I-section defined as:

$$A_f = 2 B_f t_f, \tag{16}$$

and $\tau_{y,f}$ is the shear yield stress of the flange. The term in the square brackets in Eq. (15) reduces the flange contribution in shear due to the coexisting moment within the cross-section, similar to Eq. (6). Values of the shear area reduction factor for the flanges, which are back-calculated from the FE results and denoted as $\beta_{f,d,FE}$, are plotted in Fig. 9 against the cross-section slenderness $\lambda_{\tau,cs}$. The plots in Fig. 9(a) clearly indicate that $\beta_{f,d,FE}$ reduces with increasing slenderness $\lambda_{\tau,cs}$, albeit with some scatter in the results. This scatter is reduced by accounting for the observation that the stress distribution across the flange width is more uniform with lower B_f/h_w values, and that $\beta_{f,d,FE}$ is also linked with t_f/t_w, as shown in Fig. 18(b) by plotting $\beta_{f,d,FE} B_f t_w / \left(h_w t_f\right)$ versus $\lambda_{\tau,cs}$. With the reduced scatter in Fig. 18(b), an expression to predict $\beta_{f,d,prop}$ is proposed thus:

$$\beta_{f,d,prop} = \left(\frac{0.03}{\lambda_{\tau,cs}}\right)^2 \frac{h_w t_f}{B_f t_w}. \tag{17}$$

The performance of the predictive expression is evaluated by plotting the predicted $\beta_{f,d,prop}$ against the back-calculated $\beta_{f,d,FE}$ values in Fig. 19 for the cases where $M_{Ed} < M_{f,Rd}$. Using the predictive expression in Eq. (17), the mean ratio of $\beta_{f,d,prop}/\beta_{f,d,FE}$ is 0.90, with a coefficient of variation (COV) of 0.276. The proposed expression is therefore considered to be able to predict the shear contribution of the flanges with sufficient accuracy.

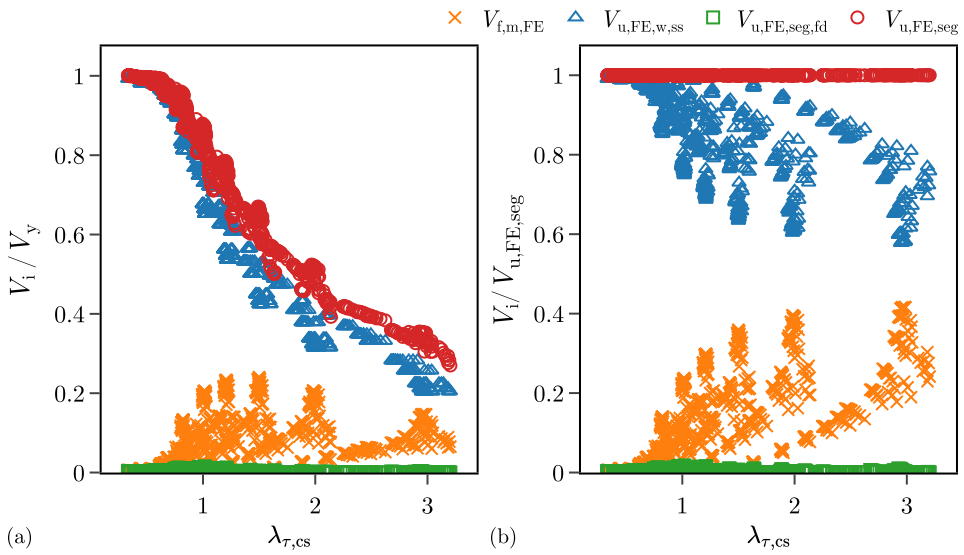


Fig. 16. (a) Ultimate shear resistance V_i, where i is indicated in the legend, normalised by V_y versus $\lambda_{\tau,cs}$; circles indicate the ultimate resistance predicted in the FE segment models, $V_{u,FE,seg}$; triangles indicate the SS results, $V_{w,ss,FE}$; squares indicate the direct contribution of the flange in shear, $V_{f,d,FE}$; crosses indicate the flange membrane contribution, $V_{f,m,FE}$; (b) contribution of flange membrane resistance and isolated web resistance relative to $V_{u,FE,seg}$.

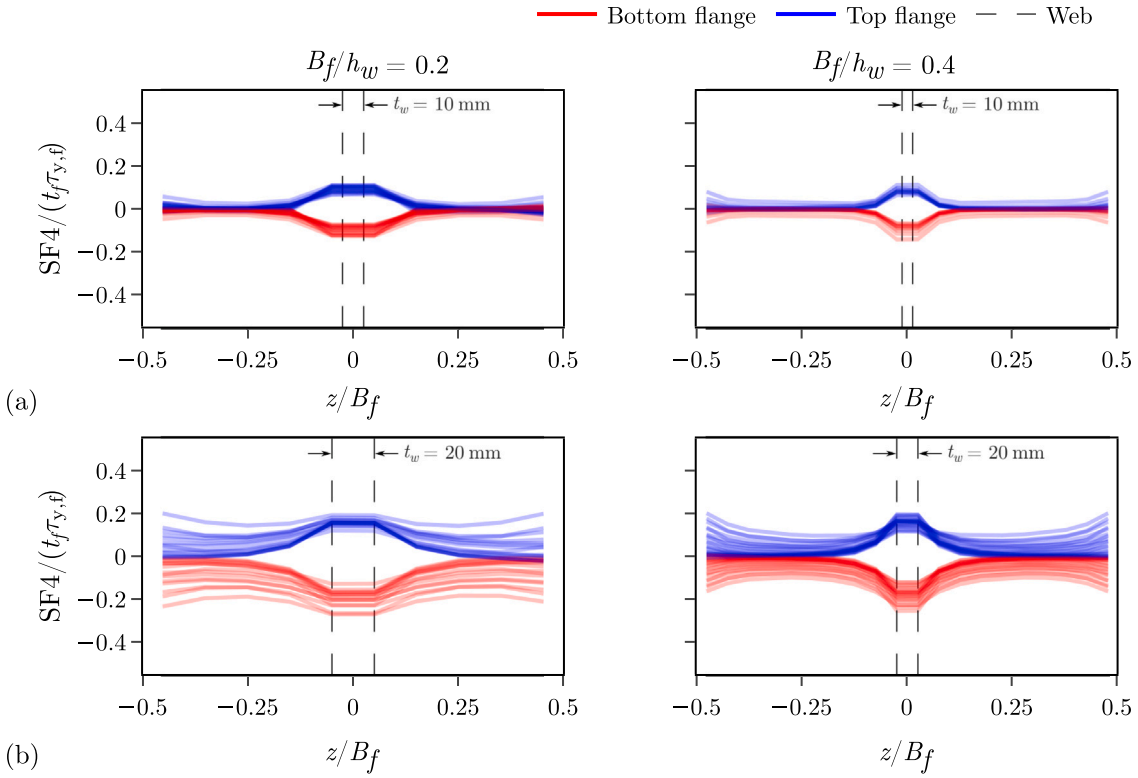


Fig. 17. Variation of normalised stress across top and bottom flange width at ultimate load for FE models when t_w is: (a) 10 mm and (b) 20 mm, with B_f/h_w as indicated; recall 'SF4' is the shear force through the thickness of the flange at $x = a/2$.

5.2. Predicting the web contribution, $V_{b,w,ss,prop}$

The response of the simply-supported isolated web under shear is examined next. The results of the shear resistance of a simply-supported web plate $V_{u,w,ss,FE}$ obtained from the parametric study on the 'isolated panel' FE model are plotted against the slenderness of the isolated panel $\lambda_{\tau,ss}$ in Fig. 20(a). The predictions from the rotated stress field method for the case of non-rigid end posts, calculated in accordance with the design recommendations of EN 1993-1-5 [12] presented in Table 3, are superimposed with dashed lines onto the plot in Fig. 20(a). For S355 grade steel, as examined in the parametric study described in Table 2, a strain hardening coefficient of $\eta = 1.2$ is recommended in EN 1993-1-5 [12]. Yet, despite specifying the QLM model (where strain hardening is accurately represented) for all the FE models considered, the strain hardening effect when $\lambda_{\tau,ss} < 1$ is not as evident as suggested in [12,13] when the web panel is modelled in isolation; hence, $\eta = 1$ is used in the plot shown in Fig. 20. Strain hardening would be expected to be influential for webs of more compact proportions (i.e. lower h_w/t_w ratios), as seen for structural elements in compression and bending [40,41], but these are not the focus of the present study.

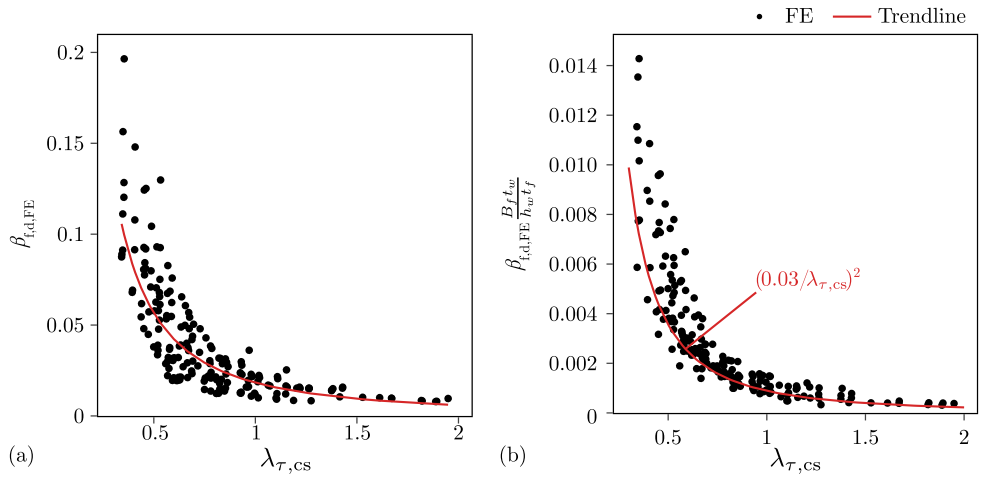


Fig. 18. Variation of (a) the flange area reduction coefficient $\beta_{f,d,FE}$ and (b) $\beta_{f,d,FE}B_f t_w/(h_w t_f)$ with $\lambda_{\tau,cs}$.

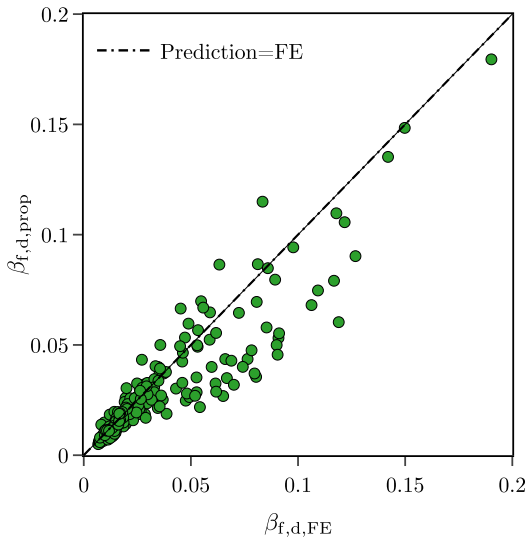


Fig. 19. Predicted $\beta_{f,d,prop}$ versus FE back-calculated $\beta_{f,d,FE}$.

The EN 1993-1-5 [12] non-rigid shear buckling curve generally over-predicts the resistances of the isolated webs with simply-supported boundary conditions (see Fig. 20(a)), but, as shown in Fig. 20(b), provides generally good predictions of the resistances determined from the 'segment' model. Thus, the current EN 1993-1-5 [12] shear buckling curve (i.e. the expressions for $\chi_{w,EC3}$ presented in Table 3) are not suitable for the methodology presented herein. Hence, a revised expression for predicting the resistance of the isolated web is proposed:

$$V_{w,ss,prop} = \chi_{w,ss,prop} V_y, \tag{18}$$

where $\chi_{w,ss,prop}$ is defined thus:

$$\chi_{w,ss,prop} = \begin{cases} \dfrac{1}{\left(\lambda_{\tau,cs}^4 + \alpha\right)^{0.5}} & \text{for } \lambda_{\tau,cs} < 1, \\ \dfrac{1}{\lambda_{\tau,cs}\left(1+\alpha\right)^{0.5}} & \text{for } \lambda_{\tau,cs} \geq 1, \end{cases} \tag{19}$$

and α is an imperfection factor that may change with material and different manufacturing tolerance; a value of $\alpha = 1.0$ is proposed for the parameters presented in this study. The proposed expression is plotted in Fig. 20, and is seen to predict the isolated web resistance effectively for all slenderness values.

5.3. Predicting the flange membrane contribution, $V_{b,f,m,prop}$

Having determined the ultimate shear capacity of the web panel in isolation $V_{w,ss,prop}$, the flange membrane contribution is back-calculated from the FE 'segment' model results $\chi_{f,m,FE}$, using the expression:

$$\chi_{f,m,FE} = \frac{V_{u,FE,seg} - V_{u,FE,seg,fd} - V_{w,ss,prop}}{V_y}, \tag{20}$$

where $V_{u,FE,seg}$ is the ultimate shear resistance determined from the parametric study on the 'segment' model and $V_{w,ss,prop}$ is calculated from Eqs. (18)–(19). For the consistency and accuracy of the proposal, the direct shear stress contribution of the flanges extracted from the FE results of the 'segment' model, $V_{u,FE,seg,fd}$, is also subtracted from $V_{u,FE,seg}$ in Eq. (20), despite being rather small, as shown in Fig. 16.

The relationship between $\chi_{f,m,FE}$ and $\lambda_{\tau,cs}$ is depicted in Fig. 21(a), where $\chi_{f,m,FE}$ is seen to increase as $\lambda_{\tau,cs}$ increases; this further evidences that $\chi_{f,m,FE}$ is more significant for more slender cross-sections. Apart from $\lambda_{\tau,cs}$, additional parameters are seen to influence the flange membrane contribution, such as the panel aspect ratio a/h_w, and the relative cross-sectional area of the web to the cross-sectional area of the flanges A_w/A_f. The influence of these parameters is demonstrated in Fig. 21(b) where $\chi_{f,m,FE}$ is plotted against the parameter $\left(\lambda_{\tau,cs} + 1/\lambda_{\tau,cs}^4 + h_w/a + 0.25A_w/A_f\right)^{-1}$, which contains a derived combination of the key influential variables. This manipulation dramatically reduces the scatter of the results, and thus the predictive function for $\chi_{f,m,prop}$ is established by conducting a linear regression analysis, resulting in the following expression:

$$\chi_{f,m,prop} = \frac{1}{3\left(\lambda_{\tau,cs} + 1/\lambda_{\tau,cs}^4 + h_w/a + 0.25A_w/A_f\right)}. \tag{21}$$

The proposed expression in Eq. (21) is evaluated by plotting the predicted $\chi_{f,m,prop}$ values against those back-calculated from the FE results in Fig. 22. A total of 1155 samples were examined, which is an increased sample size when compared to the number used in Section 5.1 due to the fact that no coexisting moment is applied to the segment models, therefore fewer results were filtered out from the parametric study presented in Table 2. Using the predictive expression in Eq. (21), the mean ratio of $\chi_{f,m,prop}/\chi_{f,m,FE}$ is 0.92, with a COV of 0.166.

5.4. Evaluation of $V_{b,prop}$ and comparison with EN1993-1-5

As discussed in Section 1, the EN 1993-1-5 expressions, presented in Eqs. (3)–(8), were calibrated to experimental results which included a co-existent moment. Therefore, the predictions using $V_{b,prop}$, presented

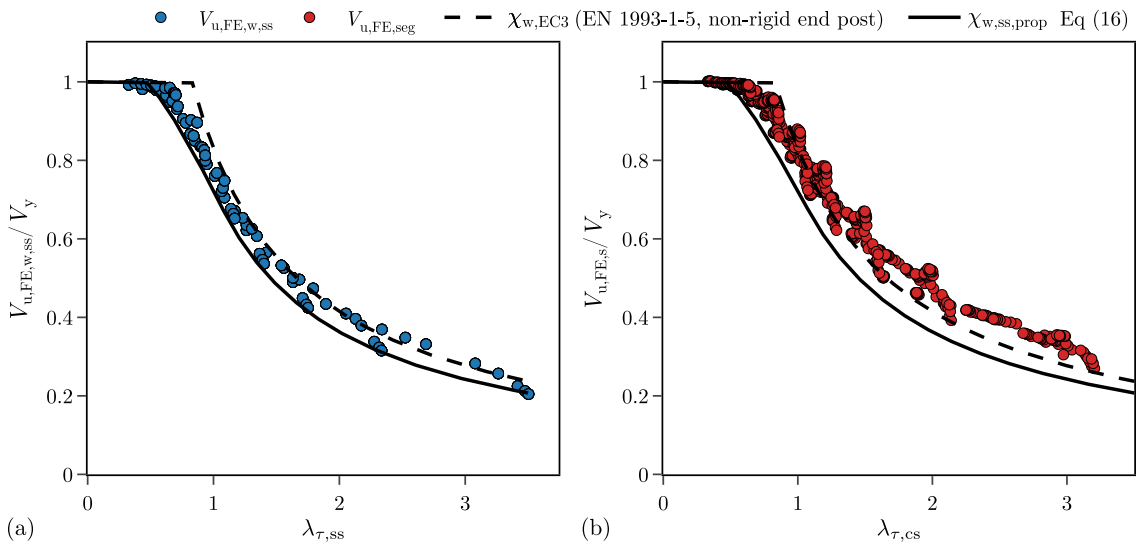


Fig. 20. (a) Normalised shear resistance of simply-supported isolated web model $V_{u,FE,w,ss}/V_y$ versus $\lambda_{\tau,ss}$, (b) normalised shear resistance of the I-section segment-model $V_{u,FE,s}/V_y$ versus $\lambda_{\tau,cs}$. The EN 1993-1-5 shear buckling reduction factor $\chi_{w,EC3}$ for the case of non-rigid end posts presented in Table 3 herein is plotted with a 'dashed' line, while the shear buckling reduction factor $\chi_{w,ss,prop}$ accounting for the cross-section slenderness presented in Eq. (19).

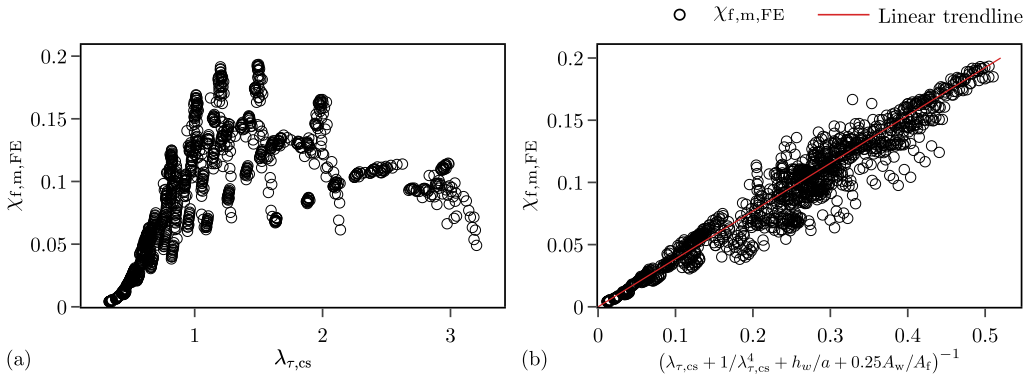


Fig. 21. Variation of $\chi_{f,m,FE}$ with (a) $\lambda_{\tau,cs}$ and (b) $\left(\lambda_{\tau,cs}+1/\lambda_{\tau,cs}^4+h_w/a+0.25A_w/A_f\right)^{-1}$.

in Eqs. (13)–(19) and Eq. (21), as well as the EN 1993-1-5 predictions are compared with the results of the full girder FE model $V_{u,FE,g}$ in Fig. 23. The results are limited to cases where $M_{Ed} < M_{f,Rd}$ and to cross-sections with flanges classified as class 1 or 2, as discussed in Section 3. The mean predicted-to-FE resistance ratio $V_{b,prop}/V_{u,FE,g}$ is 0.91, with a COV of 0.06, compared with the normalised EN 1993-1-5 prediction $V_{b,Rd,EC3}/V_{u,FE,g}$ that has a mean value of 0.87 and a COV of 0.11. The proposed expressions are consistently more accurate with a reduced scatter relative to the EC3 provisions. In the light of these findings, the proposed functions are deemed to be highly effective in predicting the shear resistance of I-section profiles under shear. Since the proposed functions have been formulated based on FE analyses performed within the parametric range described in Table 2, the recommended scope of application of the model is also limited to this range, alongside the limitations of the proposed formulae as discussed.

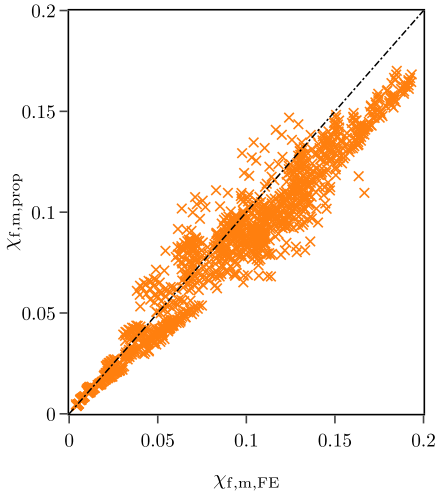


Fig. 22. Comparison of predicted $\chi_{f,m,prop}$ values and back-calculated $\chi_{f,m,FE}$ values.

5.5. Reliability analysis

In the current section, a statistical analysis of the proposed shear design expressions is conducted in accordance with the first order reliability method set out in Annex D of EN 1990 [23], to determine whether the Eurocode structural reliability requirements are met. The procedure described in [42] has been followed, as successfully implemented in several previous studies [37,43,44].

The procedure relies on knowledge of the statistical variation of the material and geometric properties, that are provided in Annex E

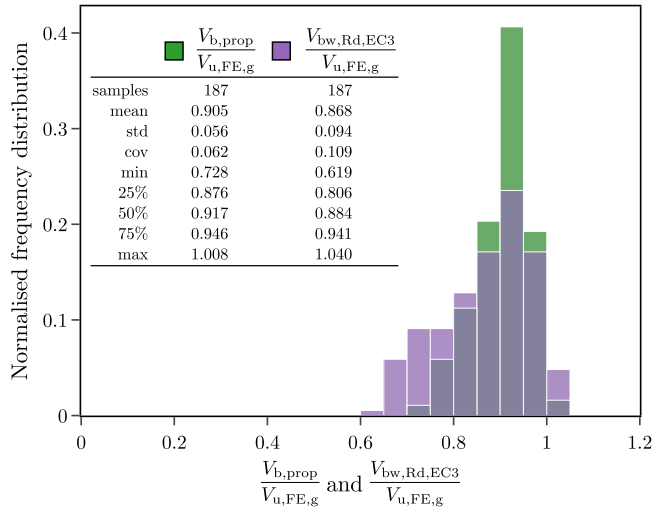


Fig. 23. Normalised frequency distribution comparing $V_{b,prop}/V_{u,FE,g}$ and $V_{bw,Rd,EC3}/V_{u,FE,g}$.

of prEN 1993-1-1:2020 [45]. Thus, the ratio between the mean and nominal yield strength of the material $\sigma_{y,m}/\sigma_{y,n}$ is taken as 1.2 for S355 steel, which has been considered in the present study, with the corresponding COV of the yield strength $V_{\sigma y}$ taken Sequal to 0.05. The Young's modulus is taken to be equal to 210 kN/mm^2, and its COV, V_E, as 0.03. The flange width B_f, the thickness of the web t_w and the overall section height H are taken as the nominal values, while the flange thickness t_f is taken as 0.98 of the nominal flange thickness $t_{f,n}$, in accordance with Annex E of prEN 1993-1-1:2020 [45]. Since H is equal to the nominal overall section depth, the web height h_w is adjusted with variations in the thickness of the flange. The COV of the cross-section geometry V_G is taken as 0.027, computed using the procedure described by Afshan et al. [42].

The proposed shear design formula given in Eq. (13) depends on the reduction factors $\chi_{w,ss}, \chi_{f,m}$ and $\beta_{f,d}$, the shear yield stress of the web and flange material and the cross-sectional area of the I-section. Since the geometry and yield stress feature in the reduction factors, they are not independent variables in the design expressions. The methodology described in Annex D of EN 1990 [23] assumes independent variables, which must therefore be separated before the reliability analysis can be applied [42]. Furthermore, a modified mean value correction factor b_c for the analysis is used and is defined as:

$$b_c = \frac{1}{n_s}\sum_{i=1}^{n_s}\frac{r_{e,i}}{r_{t,i}}, \tag{22}$$

where n_s is the number of samples, $r_{e,i}$ is the result from the FE model and $r_{t,i}$ is the predicted result using Eq. (13) for the case i considered [44]. The expression in Eq. (22) is recommended as an alternative to the least squares approach given in EN 1990, since the latter tends to bias the response towards test and FE resistances with numerically larger values [44]. The results were separated by cross-section slenderness into two groups, $0.3 \le \lambda_{\tau,cs} \le 1$ and $1 < \lambda_{\tau,cs} \le 3$. The target value of γ_{M1} is equal to unity for stability design in EN 1993-1-1. Following this procedure, the number of samples n_s is 187 and hence $k_{d,n} = 3.143$, and the relevant values from the reliability analysis of Eq. (13) are presented in Table 4, with a maximum resulting required partial safety factor of $\gamma^*_{M1} = 0.959$. Thus the expressions are considered satisfactory in terms of the first order reliability method, and a partial safety factor $\gamma_{M1} = 1.0$ can be implemented.

Table 4
Reliability analysis outcomes for proposed expressions.

$\lambda_{\tau,cs}$	b_r	V_δ	V_r	γ^*_{M1}
$0.3 \le \lambda_{\tau,cs} \le 1$	1.053	0.040	0.050	0.959
$1 < \lambda_{\tau,cs} \le 3$	1.093	0.025	0.041	0.934

5.6. Summary of proposals

The proposed formulae and procedure from the current article are summarised in Fig. 24, accounting for the partial safety factor γ_{M1}, to facilitate their implementation in practical designs. The proposed functions are different from the current Eurocode expressions in a number of ways. Since the proposed functions have been formulated based on FE analyses performed within the parametric range described in Table 2, their recommended scope of application is also limited to this range. Further investigations to explore a wider range of cross-section proportions and I-section geometries will be conducted in future work.

6. Worked example

Consider the I-section girder depicted in Fig. 3 with the following geometric and material properties: $h_w = 1000$ mm, $t_w = 6$ mm, $a/h_w = 5$, $t_f/t_w = 5$, and $B_f/h_w = 0.4$, $E = 210$ kN/mm^2, $\nu = 0.3$ and $\sigma_y = 355$ N/mm^2. The shear buckling resistance of the section is calculated as follows.

Step 1: Calculate $\tau_{cr,cs}$. The elastic buckling stress of the cross-section in shear is determined first using the expressions developed in [18]. The elastic shear buckling coefficients k_τ are calculated using centreline geometry. For the flange, $a/b_f = 25$ and therefore:

$$k^{SS}_{\tau,f} = 3.56 + 22/\left(a/b_f\right)^{3/2} = 3.56 + 22/(25^{3/2}) = 3.74, \tag{23}$$

$$k^{F}_{\tau,f} = 10 + 2.54/\left(a/b_f\right)^{3} = 10 + 2.54/(25^{3}) = 10.00, \tag{24}$$

while for the web, $a/h_w = 5$, hence:

$$k^{SS}_{\tau,w} = 5.34 + 4\left(h_w/a\right)^2 = 5.34 + 4\,(0.2)^2 = 5.50, \tag{25}$$

$$k^{F}_{\tau,w} = 8.98 + 5.60\left(h_w/a\right)^2 - 1.99\left(h_w/a\right)^3 = 8.98 + 5.60\,(0.2)^2 - 1.99\,(0.2)^3 = 9.19. \tag{26}$$

The elastic shear buckling stresses of the isolated flange and web plates are determined thus:

$$\tau^{SS}_{cr,f} = 3.74\frac{\pi^2 \times 210 \times 10^3}{12\left(1-0.3^2\right)}\left(\frac{30}{200}\right)^2 = 15{,}954.60 \text{ N/mm}^2, \tag{27}$$

$$\tau^{F}_{cr,f} = 10.00\frac{\pi^2 \times 210 \times 10^3}{12\left(1-0.3^2\right)}\left(\frac{30}{200}\right)^2 = 42{,}705.71 \text{ N/mm}^2, \tag{28}$$

$$\tau^{SS}_{cr,w} = 5.50\frac{\pi^2 \times 210 \times 10^3}{12\left(1-0.3^2\right)}\left(\frac{6}{1030}\right)^2 = 35.42 \text{ N/mm}^2, \tag{29}$$

$$\tau^{F}_{cr,w} = 9.19\frac{\pi^2 \times 210 \times 10^3}{12\left(1-0.3^2\right)}\left(\frac{6}{1030}\right)^2 = 59.18 \text{ N/mm}^2, \tag{30}$$

from which $\tau^{SS}_{cr,p} = 35.42$ N/mm^2 and $\tau^{F}_{cr,p} = 59.18$ N/mm^2 are established. For the cross-section considered, $\beta_{\tau,f} = 10$ and $\beta_{\tau,w} = 1$, thus, ϕ_τ is determined as:

$$\phi_\tau = \frac{\beta_{\tau,f}\tau^{SS}_{cr,f}}{\beta_{\tau,w}\tau^{SS}_{cr,w}} = \frac{10 \times 15954.60}{35.42} = 4504.00$$
$$\left(\phi_\tau \ge 1 \therefore \text{web is critical}\right). \tag{31}$$

For web-critical sections:

$$\zeta_\tau = 1 - \left(\frac{0.8}{\sqrt{\phi_\tau}}\frac{t_f h_w}{t_w b_f}\right) = 1 - \left(\frac{0.8}{\sqrt{4504.00}} \times \frac{5}{0.2}\right) = 0.702, \tag{32}$$

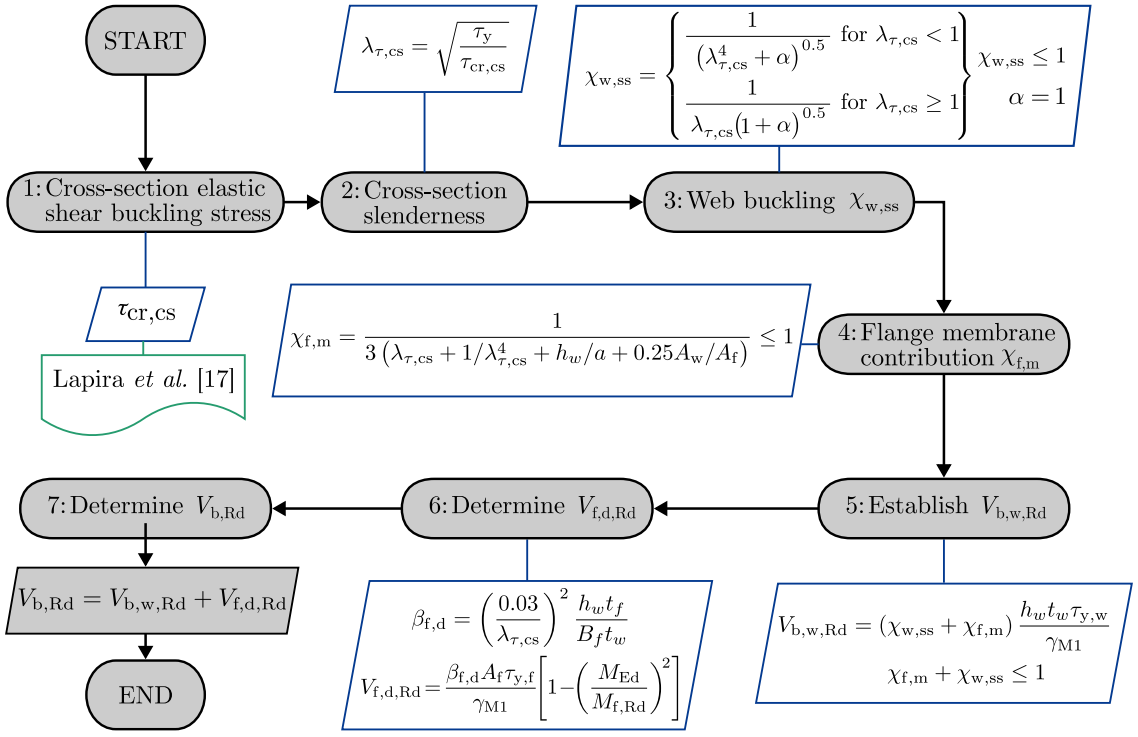


Fig. 24. Summary of proposed formulae and calculation steps to determine $V_{b,Rd}$.

and therefore the elastic buckling stress of the cross-section in shear $\tau_{cr,cs}$ is:

$$\tau_{cr,cs} = \tau_{cr,p}^{SS} + \zeta_\tau \left(\tau_{cr,p}^{F} - \tau_{cr,p}^{SS}\right) = 35.42 + 0.702\,(59.18 - 35.42)$$
$$= 52.10 \text{ N/mm}^2. \tag{33}$$

Step 2: Calculate $\lambda_{\tau,cs}$. The non-dimensional slenderness of the cross-section in shear $\lambda_{\tau,cs}$ is established using the formula:

$$\lambda_{\tau,cs} = \sqrt{\frac{\tau_y}{\tau_{cr,cs}}} = \sqrt{\frac{355/\sqrt{3}}{52.10}} = 1.98. \tag{34}$$

Step 3: Determine $\chi_{w,ss}$. The shear buckling coefficient of the web with simply-supported boundary conditions $\chi_{w,ss}$ is determined using the expressions from Eq. (19), substituting in the non-dimensional slenderness of the cross-section $\lambda_{\tau,cs}$. For the current example:

$$\chi_{w,ss} = \left[\frac{1}{\lambda_{\tau,cs}\,(1+\alpha)^{0.5}}\right] = \frac{1}{1.98\sqrt{2}} = 0.357. \tag{35}$$

Step 4: Determine $\chi_{f,m}$. The flange membrane contribution to the shear resistance of the web is evaluated using Eq. (21), reproduced thus:

$$\chi_{f,m} = \frac{1}{3\left(\lambda_{\tau,cs} + 1/\lambda_{\tau,cs}^4 + h_w/a + 0.25A_w/A_f\right)}$$

where the area of the flanges $A_f = 2B_f t_f = 24000$ mm^2 and the area of the web $A_w = h_w t_w = 6000$ mm^2. Thus:

$$\chi_{f,m} = \frac{1}{3\left[1.98 + \frac{1}{1.98^4} + \frac{1}{5} + 0.25\frac{6000}{24000}\right]} = 0.144. \tag{36}$$

Step 5: Determine $V_{b,w,Rd}$. Having evaluated $\chi_{w,ss}$ and $\chi_{f,m}$, $V_{b,w,Rd}$ is determined thus:

$$V_{b,w,Rd} = (\chi_{w,ss} + \chi_{f,m})\frac{\tau_{y,w} h_w t_w}{\gamma_{M1}} \quad \text{for } (\chi_{w,ss} + \chi_{f,m}) \leq 1$$
$$= (0.357 + 0.144)\frac{\left(0.355/\sqrt{3}\right) \times 6 \times 1000}{1.0} = 616.11 \text{ kN}. \tag{37}$$

Step 6: Determine $V_{f,d,Rd}$. The direct flange contribution to the shear resistance of the cross-section is evaluated next. First the shear area reduction factor for the flanges is found using the expression:

$$\beta_{f,d} = \left(\frac{0.03}{\lambda_{\tau,cs}}\right)^2 \frac{h_w t_f}{B_f t_w}$$
$$= \left(\frac{0.03}{1.98}\right)^2 \frac{1000 \times 30}{400 \times 6} = 2.86 \times 10^{-3}, \tag{38}$$

thus, considering the flange contribution at $x = a/2$ where $M_{Ed} = 1693.43$ kN m:

$$V_{f,d,Rd} = \frac{\beta_{f,d}\tau_{y,f} A_f}{\gamma_{M1}}\left[1 - \left(\frac{M_{Ed}}{M_{f,Rd}}\right)^2\right]$$
$$= \frac{2.86 \times 10^{-3} \times \left(0.355/\sqrt{3}\right) \times 24000}{1.0}\left[1 - \left(\frac{1693.43}{4016.23}\right)^2\right]$$
$$= 11.57 \text{ kN}. \tag{39}$$

Step 7: Determine $V_{b,Rd}$. The shear resistance of the cross-section is finally determined using the expression:

$$V_{b,Rd} = V_{b,w,Rd} + V_{f,d,Rd} = 616.11 + 11.57 = 627.38 \text{ kN}. \tag{40}$$

The resistance of the cross-section is thus $V_{b,Rd} = 627.38$ kN, which is 7% below the corresponding FE model result of $V_{FE} = 677.37$ kN. The shear resistance of the girder calculated according to EN 1993-1-5 is $V_{b,Rd,EC3} = 494$ kN, which is 27% below the corresponding FE result.

7. Conclusions

Following an assessment of the current design methods provided in EN 1993-1-5, a revised design model for determining the ultimate

shear resistance of thin-walled I-sections has been proposed presently. The shear resistance is derived from four components: (1) the shear resistance of a simply-supported web; (2) an increased web buckling stress due to the flexural restraint provided by the flange; (3) an increased web post-buckling resistance due to the membrane restraint provided by the flange; and (4) a direct contribution of the flanges to the shear resistance. Each of the components was analysed through FE models with increasing complexity, which in turn were validated against published experimental results from the literature. Closed-form expressions for predicting the direct flange contribution in shear and the flange membrane contribution have been presented, which form an integral part of the proposed formulation for determining the ultimate shear capacity of the I-section. A statistical analysis of the proposed formulae, in accordance with EN 1990 [23], was conducted, and has verified the reliability of the design recommendations. A worked example demonstrating the applicability of the proposed formulae for practical designs was also presented. When compared with the current approach within EN 1993-1-5, the newly proposed formulae predict the shear resistance of the cross-section with substantially greater accuracy and consistency. In continuation of this research on the structural behaviour of girders, the authors are currently engaged in extending the methodology to encompass girders with warped webs, as part of their ongoing research into the structural behaviour of such girders [6]. Additionally, the authors are also considering girders with diverse end-conditions, including rigid end posts, in order to establish a comprehensive understanding of their effects.

CRediT authorship contribution statement

Luke Lapira: Writing – original draft, Conceptualization, Formal analysis, Investigation, Methodology, Validation, Visualization. **Leroy Gardner:** Writing – review & editing, Supervision, Investigation, Conceptualization. **M. Ahmer Wadee:** Writing – review & editing, Supervision, Investigation, Conceptualization.

Declaration of competing interest

The authors declare that they have no known competing financial interests or personal relationships that could have appeared to influence the work reported in this paper.

Data availability

Data will be made available on request.

Acknowledgement

Financial support for Luke Lapira was provided by the President's PhD Scholarship scheme from Imperial College London, United Kingdom.

References

[1] J.M. Wilson, On specifications for strength of iron bridges, Trans. Am. Soc. Civ. Eng. 15 (1886) 389–414, http://dx.doi.org/10.1061/TACEAT.0000597.
[2] H. Wagner, Flat Sheet Metal Girders with Very Thin Metal Web. Part I: General Theories and Assumptions, NACA T.M. 604, Washington, D. C., 1931.
[3] K. Basler, Strength of plate girders in shear, ASCE J. Struct. Div. 87 (1961) 151–180.
[4] D.M. Porter, K.C. Rockey, H.R. Evans, Collapse behaviour of plate girders loaded in shear, Struct. Eng. 53 (1975) 313–325.
[5] T. Höglund, Simply supported long thin plate I-girders without web stiffeners subjected to distributed transverse load, in: IABSE Colloquium London, Articles of the Working Comissions, 1971, pp. 85–97.
[6] L. Lapira, M.A. Wadee, L. Gardner, Nonlinear analytical modelling of flat and hyperbolic paraboloidal plates under shear, Proc. R. Soc. A 477 (2253) (2021) 20210317, http://dx.doi.org/10.1098/rspa.2021.0317.
[7] S.C. Lee, C.H. Yoo, Experimental study on ultimate shear strength of web panels, ASCE J. Struct. Eng. 125 (8) (1999) 838–846, http://dx.doi.org/10.1061/(ASCE)0733-9445(1999)125:8(838).
[8] Y.B. Kwon, S.W. Ryu, The shear strength of end web panels of plate girders with tension field action, Thin-Walled Struct. 98 (2016) 578–591, http://dx.doi.org/10.1016/j.tws.2015.11.002.
[9] D.R. Hingnekar, A.Y. Vyavahare, Mechanics of shear resistance in steel plate girder: critical review, ASCE J. Struct. Eng. 146 (6) (2020) 03120001–1–03120001–16, http://dx.doi.org/10.1061/(ASCE)ST.1943-541X.0002484.
[10] P. Kuhn, J.P. Peterson, L.R. Levin, A Summary of Diagonal Tension. Part I: Methods of Analysis, NACA T.N. 2661, National Advisory Committee for Aeronautics, Langley Field, VA, 1952, http://dx.doi.org/10.1097/00152192-198911000-00004.
[11] T. Höglund, Shear buckling resistance of steel and aluminium plate girders, Thin-Walled Struct. 29 (1997) 13–30, http://dx.doi.org/10.1063/1.329413.
[12] E. 1993-1-5, Eurocode 3 - Design of Steel Structures – Part 1-5: Plated Structural Elements, European Committee for Standardisation (CEN), Brussels, Belgium, 2006.
[13] B. Johansson, R. Maquoi, G. Sedlacek, C. Müller, D. Beg, Commentary and Worked Examples to EN 1993-1-5 "Plated Structural Elements", JRC Scientific and Technical Reports, European Communities, 2007.
[14] C.H. Yoo, S.C. Lee, Mechanics of web panel postbuckling behavior in shear, ASCE J. Struct. Eng. 132 (2006) 1580–1589, http://dx.doi.org/10.1061/(ASCE)0733-9445(2006)132.
[15] S.C. Lee, D.S. Lee, C.H. Yoo, Further insights into postbuckling of web panels. I: Review of flange anchoring mechanism, ASCE J. Struct. Eng. 135 (2009) 3–10, http://dx.doi.org/10.1061/(ASCE)0733-9445(2009)135:1(3).
[16] S.C. Lee, D.S. Lee, C.S. Park, C.H. Yoo, Further insights into postbuckling of web panels. II: Experiments and verification of new theory, ASCE J. Struct. Eng. 135 (2009) 11–18, http://dx.doi.org/10.1061/(ASCE)0733-9445(2009)135:1(11).
[17] S.C. Lee, C.H. Yoo, Strength of plate girder web panels under pure shear, ASCE J. Struct. Eng. 124 (1998) 184–194, http://dx.doi.org/10.1061/(asce)0733-9445(1999)125:1(115.2).
[18] L. Lapira, L. Gardner, M.A. Wadee, Elastic local buckling formulae for thin-walled I-sections subjected to shear and direct stresses, Thin-Walled Struct. 182 (2023) 110150, http://dx.doi.org/10.1016/j.tws.2022.110150.
[19] C. Scandella, M. Neuenschwander, K.M. Mosalam, M. Knobloch, M. Fontana, Structural behavior of steel-plate girders in shear: Experimental study and review of current DesignPrinciples, J. Struct. Eng. 146 (11) (2020) 04020243, http://dx.doi.org/10.1061/(ASCE)ST.1943-541X.0002804.
[20] K.E. Augustyn, S.E. Quiel, M. Garlock, Post-buckling shear resistance of slender girder webs: Stiffener participation and flange contributions, J. Constr. Steel Res. 190 (2022) 107117, http://dx.doi.org/10.1016/j.jcsr.2021.107117.
[21] K.E. Augustyn, S.E. Quiel, M. Garlock, Formation of post-buckling shear mechanisms in stiffened web panels of slender steel plate girders, Thin-Walled Struct. 184 (2023) 110481, http://dx.doi.org/10.1016/j.tws.2022.110481.
[22] Dassault Systèmes Simulia Corp, ABAQUS/Standard Version 2021, Providence, RI, USA, 2021.
[23] EN 1990:2002+A1:2005, Eurocode: Basis of Structural Design, European Committee for Standardisation (CEN), Brussels, Belgium, 2005.
[24] D.A. Nethercot, M.P. Byfield, Calibration of design procedures for steel plate girders, Adv. Struct. Eng. 1 (2) (1997) 111–126, http://dx.doi.org/10.1177/136943329700100203.
[25] X. Yun, L. Gardner, Stress–strain curves for hot-rolled steels, J. Constr. Steel Res. 133 (2017) 36–46, http://dx.doi.org/10.1016/j.jcsr.2017.01.024.
[26] L. Gardner, X. Yun, Description of stress–strain curves for cold-formed steels, Constr. Build. Mater. 189 (2018) 527–538, http://dx.doi.org/10.1016/j.conbuildmat.2018.08.195.
[27] O. Zhao, L. Gardner, B. Young, Behaviour and design of stainless steel SHS and RHS beam-columns, Thin-Walled Struct. 106 (2016) 330–345.
[28] B. Behzadi-Sofiani, L. Gardner, M.A. Wadee, Testing, simulation and design of steel equal-leg angle section beams, Thin-Walled Struct. 171 (2022) 108698.
[29] J. Wang, L. Gardner, Flexural buckling of hot-finished high-strength steel SHS and RHS columns, J. Struct. Eng. 143 (2017) 04017028, http://dx.doi.org/10.1061/(ASCE)ST.1943-541X.0001763.
[30] P. Kyvelou, L. Gardner, D.A. Nethercot, Finite element modelling of composite cold-formed steel flooring systems, Eng. Struct. 158 (2018) 28–42, http://dx.doi.org/10.1016/j.engstruct.2017.12.024.
[31] E. Riks, An incremental approach to the solution of snapping and buckling problems, Int. J. Solids Struct. 15 (7) (1979) 529–551, http://dx.doi.org/10.1016/0020-7683(79)90081-7.
[32] G.B. dos Santos, L. Gardner, M. Kucukler, A method for the numerical derivation of plastic collapse loads, Thin-Walled Struct. 124 (2018) 258–277, http://dx.doi.org/10.1016/j.tws.2017.11.055.
[33] prEN 1993-1-14:2020, Eurocode 3 – Design of Steel Structures – Part 1-14: Design Assisted by Finite Element Analysis, European Committee for Standardisation (CEN), Brussels, Belgium, 2020.
[34] C.M. Gomes, P.J. Cruz, L.S.d. Silva, Avaliação Experimental do Comportamento ao Corte de Vigas de aço Esbeltas, Engenharia Civil UM, 2000.

[35] P. Wang, K. Augustyn, A. Gomez, S. Quiel, M. Garlock, Influence of boundary conditions on the shear post-buckling behavior of thin web plates, in: Proceedings of the Annual Stability Conference Structural Stability Research Council St. Louis, Missouri, April 2-5, 2019, 2, 2019, pp. 503–521.
[36] E. 1993-1-1:2005+A1:2014, Eurocode 3 – Design of Steel Structures – Part 1-1: General Rules and Rules for Buildings, European Committee for Standardisation (CEN), Brussels, Belgium, 2014.
[37] N. Saliba, E. Real, L. Gardner, Shear design recommendations for stainless steel plate girders, Eng. Struct. 59 (2014) 220–228, http://dx.doi.org/10.1016/j.engstruct.2013.10.016.
[38] D. Williams, B. Aalami, Thin Plate Design for In-Plane Loading, Granada, London, UK, 1979.
[39] L. Gardner, A. Fieber, L. Macorini, Formulae for calculating elastic local buckling stresses of full structural cross-sections, Structures 17 (2019) 2–20, http://dx.doi.org/10.1016/J.ISTRUC.2019.01.012.
[40] X. Yun, L. Gardner, N. Boissonnade, The continuous strength method for the design of hot-rolled steel cross-sections, Eng. Struct. 157 (2018) 179–191, http://dx.doi.org/10.1016/j.engstruct.2017.12.009.
[41] A. Liew, L. Gardner, Ultimate capacity of structural steel cross-sections under compression, bending and combined loading, Structures 1 (2015) 2–11, http://dx.doi.org/10.1016/j.istruc.2014.07.001.
[42] S. Afshan, P. Francis, N.R. Baddoo, L. Gardner, Reliability analysis of structural stainless steel design provisions, J. Constr. Steel Res. 114 (2015) 293–304, http://dx.doi.org/10.1016/j.jcsr.2015.08.012.
[43] J. Shen, M.A. Wadee, Local–global mode interaction in thin-walled inelastic rectangular hollow section struts part 2: Assessment of existing design guidance and new recommendations, Thin-Walled Struct. 145 (2019) 106184, http://dx.doi.org/10.1016/j.tws.2019.106184.
[44] X. Meng, L. Gardner, A.J. Sadowski, J.M. Rotter, Elasto-plastic behaviour and design of semi-compact circular hollow sections, Thin-Walled Struct. 148 (2020) 106486, http://dx.doi.org/10.1016/J.TWS.2019.106486.
[45] prEN 1993-1-1:2020, Eurocode 3 – Design of Steel Structures – Part 1-1: General Rules and Rules for Buildings, European Committee for Standardisation (CEN), Brussels, Belgium, 2020.